A Comprehensive Investigation on Application of Machine Learning for Optimization of Process Parameters of Laser Powder Bed Fusion Processed 316L Stainless Steel

Sulaymon Eshkabilov (sulaymon.eshkabilov@ndsu.edu)
North Dakota State University https://orcid.org/0000-0002-7266-2201
Ismat Ara
Fardad Azarmi

Research Article

Keywords: Process parameters optimization, laser powder bed fusion, Machine learning algorithm, Mechanical properties, Microstructural characterization

Posted Date: July 20th, 2022

DOI: https://doi.org/10.21203/rs.3.rs-1836867/v1

A Comprehensive Investigation on Application of Machine Learning for Optimization of Process Parameters of Laser Powder Bed Fusion Processed 316L Stainless Steel

Sulaymon Eshkabilov[a,1, 0000-0002-7266-2201], **Ismat Ara**[b, 0000-0002-9851-8849], **Fardad Azarmi**[b, 0000-0002-8904-352X]

[a] Department of Ag and Biosystems Engineering, North Dakota State University, Fargo, *ND 58108-6050, USA*
[b] Department of Mechanical Engineering, North Dakota State University, Fargo, *ND 58105-6050, USA*

Abstract

Metal 3D printing has gained a lot of attention among industries since it offers a practical solution to problems rising during manufacturing of parts and components with complex geometry. This is an additive technology that eliminated several fabrication steps and at the same time reduces material waste during manufacturing process. However, in all additive manufacturing technologies, the final properties of the parts are determined by the operational process parameters. In this study, several machine learning algorithms were examined to characterize the effects of the printing process parameters on relative density, hardness, yield strength, and tensile strength in manufactured parts. It was possible by using "Big Data" collected from a large number of previously published articles on application of Laser Powder Bed Fusion (LPBF) for 3D printing of 316L stainless steel samples. Among different process parameters, laser power, laser energy density, and scanning speed were proven to have the largest effects directly on physical and mechanical properties of LPBF processed parts. Six different classification models and five support vector machine regression-based models were tested to find the most accurate prediction algorithm. To validate the obtained results from the applied machine learning models, a set of 316L specimens were produced using LPBF technology using a random set of process parameters. The physical and mechanical properties of 3D printed samples were tested and compared to the ones those predicted from the optimum models from machine learning analysis. The results were in great agreement, which shows the high accuracy of the developed machine learning algorithms in this study.

Keywords: Process parameters optimization; laser powder bed fusion; Machine learning algorithm; Mechanical properties; Microstructural characterization.

1. INTRODUCTION

Metal Additive manufacturing (AM) technology has found its place as a reliable production technology in various industries, such as automotive, aerospace, and biomedical. It significantly reduces required production steps as needed in conventional technologies for manufacturing metallic parts and components [1-4]. It is a highly efficient method for fabrication of complex metal parts in a single step that requires less materials due to the possibility of recycling and reuse of waste metal powders and minimizing of scraps [5]. Conventional casting and other mechanical processing techniques require to undergo several stages of

[1] Address Correspondence to E-mail: sulaymon.eshkabilov@ndsu.edu, and at: Department of Ag and Biosystems Engineering, North Dakota State University, 105 ABEN, NDSU Dept. 7620, Fargo, *ND 58108-6050, USA*.

processing and the final products are usually needed to undergo a post processing step to be at desired geometry and properties [1]. However, AM technology is capable of near – net – shape fabrication of parts with elimination of extra processing stages. In many cases, there is no need for further post processing to enhance properties of the final products [2]. The capability of manufacturing components with complex geometry and rapid prototyping are among other advantages of AM technology. The flexibility of AM technology enables production of fully dense metallic parts and components with high quality [6-7]. Thus, AM technology is considered as one of the promising methods for manufacturing of small to medium metal objects with complex shapes and geometries [1-4].

Currently, there are two concepts of AM technology mainly used for commercial production of metals or metal alloys, which are *powder bed fusion*, and *directed energy deposition* processes [1]. While both of these technologies and their subcategories have their own uniqueness and applicability, selective laser melting (SLM), a Laser Powder Bed fusion (LPBF)-based technology, is among the commonly used technologies due to its high dimensional tolerance, high accuracy, good surface condition (roughness), and larger choices for feedstock materials [1, 8, 9]. LPBF uses high power laser beam to make complicated metal components by selectively fusing and consolidating the few-micron-thick powder layer [1-2]. After the rapid cooling of the melted layer, another thin layer of powder is spread over it and this process continues until the part is built [3-4].

AM technology is widely used to manufacture parts from aluminum, titanium, CoCr alloys, Fe- based alloys, Ni based alloys, tungsten, gold, and silver [10, 11]. Among these metals, stainless steel 316L is frequently applied in the biomedical, nuclear, aerospace, aeronautics, automobile, petrochemical, gas, and marine industries and is versatile due to its high corrosion resistance, oxidation resistance, strength, toughness, biocompatibility, excellent welding ability, favorable strength ductility synergy, fatigue resistance, and availability [12-18]. Achieving acceptable density and microstructure by AM for several alloys are still a challenge. However, LPBF made 316L SS was reported to achieve significant success with near full density, reasonable tensile properties, and yield strength [13]. The reason for the superior mechanical properties was attributed to the unique hierarchically heterogeneous microstructure which comprises refined columnar grains, cellular dislocation tangles, and nano-inclusions [9, 18]. As a result, extensive amount of studies and experiments are being conducted on the LPBF made 316L SS samples.

1.1. Laser Powder Bed Fusion (LPBF) Process Parameters

The final properties, such as mechanical, thermal, and electrical characteristics of the LPBF fabricated parts, significantly depend on operational processing parameters. There are several important LPBF processing parameters such as laser power, scanning speed, hatching distance, powder size, hatching angle, etc. The poor choice of processing parameter can lead to the residual stresses in this alloy which can end up forming thermal cracks and thus lead to failure [1, 19, 20]. Besides, processing parameters also affects the microstructure, which leads to difference in mechanical behavior as well. Hence, optimization of the processing parameter is an important factor for achieving high mechanical properties for LPBF made 316L SS. Many studies have been done on the optimization of process parameter for LPBF processed material including 316L SS [5, 12, 14, 15, 16, 17, 21-34]. Multiple parameters are controlled during the AM process and some important ones are reviewed here. As we know parts are made layer by layer in AM technology and therefore, the thickness of each layer plays a key role on the building rate, cooling rate, mass transfer, and heat transfer properties. While increasing the (powder) layer thickness can decrease the manufacturing time, smaller layer thickness can produce denser parts with better dimensional accuracy. It is important to manufacture parts with required thickness to provide desired properties, geometry, and performance [35, 36, 37].

Laser power is another important processing parameters and has significant impact on the microstructure, mechanical, and physical properties. The average grain size was found to be increased from 25 to 65 μm with the increase of laser power from 120 W to 220 W [12]. When the laser power is increased from 129 W to 189 W, yield strength was increased from 265 MPa to 524 MPa and ultimate tensile strength was reported to be increased from 280 MPa to 647 MPa [38]. The unmelted powder in the voids of the metal produced at lower laser power is the reason for the inferior mechanical properties [12, 38]. Increasing laser power leads to a complete melting of powder which leads to denser product at the end. Thus, the mechanical properties are usually superior at higher laser power [38]. When parts are being manufactured with the LPBF method, the laser beam is shifted from one scanning strip to the subsequent ones in a two-dimensional plane for selective melting. The distance between the center of the two subsequent stripes is called hatch spacing [1]. Hatch distance is also an important processing parameter, as the material property depends on this parameter. A relative density of 99.9 % and low average surface roughness of 2.68 μm can be achieved by an optimized hatch spacing of 100 μm [39]. At the maximum hatch distance of 70 μm the density and tensile property of LPBF made 316L SS was reported to be highest by Liverani et. al [34].

Scan speed has also been found to have significant impact on the properties of the final product as well and it is defined as the speed at which the laser scans on the build plate. The tensile properties of Co-Cr-W was reported to increase until they reach the peak at 700 mm/s, and then start to decrease with the increase of scan speed [40]. At high and low scanning speed the various kind of defects such as unmelted particles and porosity can be induced at each layer due to lack of fusion [1]. Thus, it is important to select the optimized scanning speed to achieve supreme mechanical property.

Finally, laser energy density (LED) is the most influential parameter in the LPBF process, which depends on the laser power, scanning speed, layer thickness, and hatch distance according to equation (1) [25].

$$LED = LP/(v \times t \times h) \tag{1}$$

Where *LED* is laser energy density in J/mm^3, *LP* is the laser power in W, *v* is the scanning speed in mm/s, *t* is layer thickness in mm, and *h* is the hatching distance in mm. The laser energy density alone plays a decisive role on the development of desired microstructure and optimum mechanical property during the LPBF process. Low energy density of 29.2 J/mm^3 was reported to show discontinuous laser tracks and large irregular pores in the microstructure [16]. Similarly, at high laser energy density of 233.8 J/mm^3; numerous pores and cracks were detected in the microstructure [16]. However, at an optimized laser energy density of 116.9 J/mm^3 a smooth surface with relative density of 99% could be achieved [17]. The effect of the microstructure is reflected on the mechanical properties as reported by Cherry *et al* [26]. It is found that the lowest amount of porosity was detected at 104.52 J/mm^3 among three laser energy density i.e. 41.81 J/ mm^3, 104.52 J/ mm^3, and 209.03 J/mm^3 [26]. Hence, the maximum hardness was measured for the material made at 104.52 J/mm^3 as well [26].

The application of a mathematical model using regression or a statistical analysis and mechanistic models to predict mechanical properties and performances of the AM processed parts is an emerging field of research in AM community [41]. One example of such application is possible by using Fourier heat conduction equation known as “Part scale heat conduction model”. It is applied in temperature fields of melt pool and fusion zone geometry to calculate cooling rates of 3D printed metals [41 --44]. Limitation of this model is that it does not consider the effect of molten metal flow inside the pool that severely reduces the accuracy of the calculated results. Another suggested model known as “Part Scale Heat Transfer and Fluid Flow” represent more accurate temperature distribution and deposit geometry since it takes to the account the effects of molten metal flow inside the pool [45, 46]. Part scale volume of fluid is another known model for the calculation of molten pool geometrical calculation and temperature- velocity field which tracks the free surface of the molten pool [47, 48]. However, this model was found to have errors and disagrees with the experimental results in terms of deposit shape and size [47, 48].

Several models are established for the prediction of microstructure, nucleation, and grain growth. TTT-based models (TTT diagrams provide the effects of time and temperature on microstructure development of an alloy at constant temperature), continuous cooling transformation-based models, Johnson- Mehl-Avrami models, Monte Carlo method, cellular automata, and phase field model are example of such models, which deal with the prediction of microstructure, nucleation, and grain growth [49-56]. There is finite element analysis-based model as well for the calculation of residual stresses and distortion [57, 58]. Although these mechanistic models are effective simulation tools to get insight of the AM processed parts, they all have some limitations in prediction of properties with high accuracy. The main challenge of these models is addressing the full extent of the process and parts in a mathematical format. This challenge is usually undertaken by considering the most important physical process and ignoring the least important ones. As a result, the models lack accuracy. In addition, these mechanistic models need an extensive amount of understanding of underlying physical mechanisms, significant computational resources, and they are complex.

1.2. Machine Learning Concept

Machine Learning has recently gained a lot of attention as a modelling tool for clustering, classification, prediction, and pattern recognition of large data sets in various domains of science and technology [59, 60]. Machine learning comes into play when a known mathematical derivative or formula, such as fit and regression models, fail to provide accurate results. In this method, a large data set is used as variables for several numerical predictors to extract outcomes as categorical and numerical response variables. There are mainly two dominant methods of machine learning, which are known as *supervised* and *unsupervised* learning approaches. These methods are built based on different algorithms, such as k-means, k-nearest neighbors, dendrogram, linear discriminants, support vector machines (SVM), classification trees, Naïve Bayes, AdaBoost (Ensemble Learning and Boosting), etc. [60]. Each of these algorithms work with high accuracy in specific condition and none of them is considered as a global solution, which can be used in all cases for application of machine learning [60].

As opposed to the mechanistic models, machine learning requires less mathematical formulations and models to build a model that predicts or classifies data. The machine learning can employ results from a large number of data (Big Data) and combine the effects in a logical manner to establish a relationship between input data and response (output). It has several advantages over the classical statistics and simple regression models when the accurate prediction of the responses is the main focus and when dealing with unwieldy data [61]. Machine learning uses minimal assumption and is fairly effective even when dealing with data from uncontrolled experimental design and having complicated nonlinear interactions [61]. In addition, machine learning is capable of taking up various features as predictor variables and solving several problems of mechanistic models simultaneously; for instance, to simulate temperature, velocity fields, cooling rates, and solidification, and it does not require complex mathematical formulations to model and predict the response variables in AM processed metallic parts [41]. By application of machine learning algorithm models, it is not only possible to explain the evolution of the microstructure, defects, and properties of AM parts due to the chosen process parameters and the thermophysical properties of the feedstock material but also to predict the final properties of the processed AM parts [41].

Therefore, the applications of machine learning algorithms could be an alternative solution to the problem of the optimization of the process parameter in AM. In recent years, machine learning tools have been applied in many engineering optimization and prediction problems. There are many studies where machine learning algorithms were found to be very efficient and highly accurate in classification, clustering, and predicting the response variables [41, 59-61]. Several studies have been performed to utilize machine learning in correlating process parameters of additively manufactured parts with their quality, and consequently prediction of the performance of 3D printed metallic parts.

Machine learning algorithm has been explored to optimize process parameters of AM technology to improve "on-site" and "layer-wise" control of the AM part. Silbernagel *et al.* used a machine learning algorithm to correlate the onsite images of scan tracks and images of copper test specimen made by "laser powder bed fusion" technology to its process parameters, and based on the correlation between the images and process parameters, the optimized process parameters were described [62]. Similarly, Caggiano *et al.* applied a machine learning model based on a bi-stream deep convolutional neural network (DCNN) to characterize layer-wise images of SLM processed Inconel 718 powder, and based on the characterization, defects were predicted by the machine learning algorithm [63]. The developed machine learning model was able to detect the defects in SLM layers with accuracy as high as 99.4% [63]. In addition, machine learning based algorithms have been used for the development of process map for AM processes. For example, Aoyagi *et al.* used a support vector machine learning approach to develop a process map for predicting the effective process condition for a CoCr alloy made by an electron beam powder bed fusion process [64]. They reported that the process map they developed using the SVM was able to reduce the number of experiments necessary to achieve an optimized process condition [64].

Compositional grading has been characterized with respect to process parameters using machine learning algorithm, as well. Rankouhi *et al.* applied machine learning to determine the process parameters for compositional grading of 316L-Cu multi-material, and their model provided insight about the underlying mechanism behind the nonlinear behavior between process parameters and material composition [65]. In addition, they reported that laser power and laser scanning velocity had the most influence on the part density and surface roughness using multivariate Gaussian process model with an averaged mean absolute prediction error of 1% for density prediction and 47.6% for surface roughness prediction [65]. Machine learning algorithms have also shown promise in optimizing surface characteristics and dimensional accuracy. Cao *et al*. proposed a data driven Kriging model to build a relationship between key process parameters and the surface roughness and the dimensional accuracy of the laser powder bed fusion processed 316L stainless steel [66]. Moreover, they used a whale optimization algorithm to obtain the optimal surface roughness and dimensional accuracy [66]. Another study on the optimization of surface texture was performed by Özel *et al.*, using neural network-based machine learning methods for nickel alloy (625) material processed by LPBF. They tried to develop a predictive model and alsoestablish a relationship between LPBF process parameters, such as energy density, scan strategy, and the surface texture [67]. Khanzadeh *et al.* developed a porosity prediction model using supervised machine learning for AM parts, where a relationship between melt pool and microstructural characteristics [68]. Barrionuevo *et al.* applied seven supervised machine learning regressors (support vector machine, decision tree, random forest, gradient boosting, Gaussian process, K-nearest neighbors, multi-layer perceptron) to predict the relative density of SLM processed 316L SS [69]. The multi-layer perceptron showed the best performance with R^2 of 0.6050 and K-nearest neighbors exhibited the worst performance with R^2 of 0.4851 [69]. In addition, Aboutaleb *et al.* applied multi-objective accelerated process optimization (m-APO) methodology to obtain maximum relative density and elongation-to-failure of SLM processed Ti-6Al-4V [70]. The application of proposed optimization process resulted in 51.8% reduction of experimental run times in contrast to an extended full factorial design of experimental algorithm [70].

Tensile properties of AM parts have also been predicted by machine learning algorithms. For example, Hertlein *et al.* utilized a Bayesian network to relate the process parameters such as laser power, scan speed, hatch spacing, and layer thickness with the part quality (density, hardness, top layer surface roughness, and ultimate tensile strength) of a SLM processed 316L SS [71]. In contrast to the final tensile properties of AM parts, Muhammad *et al.* focused on predicting the evolution of plastic deformation during tensile loading using machine learning [72]. Here, they proposed a machine learning based artificial neural network for predicting the evolution of local strain distribution, plastic anisotropy, and failure during tensile deformation of AlSi10Mg alloy processed by selective laser melting [72]. Some researchers have combined the machine learning algorithm with a conventional mathematical model to develop new optimization methodology. For example, Zhan *et al.* developed a new method by combining machine learning and continuum damage mechanics to predict the fatigue life of additively manufactured aerospace alloys [73].

They observed that a random forest model predicted fatigue life for the AM SS316L, TiAl6V4, and AlSi10Mg samples better than an artificial neural network, and the MAE of random forest and artificial neural network models were respectively 0.242 and 0.537 [73]. Zhang *et al.* also predicted fatigue life using machine learning algorithm, and they applied neuro-fuzzy-based machine learning approach for developing a predictive model that was able to predict the high cycle fatigue life of laser powder bed fusion processed 316L SS with an overall RMS error range from 11% to 16% across the datasets [74].

Although a wide range of studies are observed on the application of machine learning in additively manufactured metals, it seems that the studies that used process parameters to predict properties and performance of SLM processed 316L SS were not sufficiently efficient and accurate. In general, the majority of the researches in this area tried to develop a model to establish a relationship between the part characteristics, such as density, hardness, surface roughness, and tensile strength, with process parameters, such as laser power, scan speed, and hatch spacing. While there was significant improvement in establishing such relationship but the results from the application of the machine learning approach were not highly successful. One of the reasons behind the model's low accuracy was attributed to both the possibility of the non- manufacturability of the data set and the n-dimensional convex hull, which has a low prediction accuracy for the input variables outside the convex hull. In another optimization study based on machine learning approach, the algorithm was based on a theoretical foundation that related the microstructural features to the solidification mechanism and it was obvious that prediction based on this model was only applied to ideal solidification condition. The accuracy of some models was also under question due to the inconsistency in the use of the data for the optimization of the process parameters. Besides, none of the published literature on the application of machine learning algorithms on SLM processed 316L SS considered the optimization of yield strength using the process parameters. Moreover, to the best of the knowledge of the authors, there is no literature that explores extensively the validity of supervised and unsupervised learning algorithms with classification and regression machine learning routines to locate optimal values of ultimate tensile strength, yield strength, relative density, and hardness. To this end, this study is novel due to achievement of high accuracy in optimization of process parameters. The present study is also unique in terms of predicting the yield strength of SLM processed 316L SS in addition to the other properties.

1.3. Aims and Scope

As mentioned before, there is no available literature in machine learning algorithm applications to predict end mechanical properties of SLM printed 316L SS metal parts with high accuracy by proposing and comparing performances of supervised and unsupervised learning routines and models. There is no study on predicting the yield strength of the SLM processed 316L SS using machine learning approach. This study used a new method to apply a few machine learning algorithms and models with optimized parameters using training and testing data to predict the end product properties with very high accuracy. The scope of this paper is to study applicability of the machine learning's classification and regression algorithms, such as dendrogram, kNN, ensemble, and SVM with optimized hyper parameters, kernel functions, and k-fold validation options. Literature reviews on the effects of the processing parameters on the microstructural compositions and mechanical properties of LPBF processed metallic parts showed that the choice of optimum parameters is the most crucial step in any AM process. Finding necessary process parameters leading to predefined (optimized) output material properties saves a significant amount of energy, manufacturing costs, and time.

Against this backdrop, the current endeavor was to establish a more reasonable machine learning algorithm based on a reliable and large-scale data set for a broader range of material properties. The aim of the study was to develop a methodology for the unsupervised and supervised machine learning algorithms to classify and predict mechanical properties including yield strength of LPBF processed specimens in connection with the LPBF process parameters based on LPBF manufactured 316L SS data from published literature. Finally, the accuracy and validity of the proposed machine learning algorithms and models were experimentally validated by printing several 316L SS samples with a random set of the LPBF process parameter values. The physical and mechanical properties of the printed samples were experimentally measured and compared to those predicted by the developed machine learning algorithms and models.

2. EXPERIMENTAL PROCEDURE FOR VALIDATION RUN

The predictive methodology described in the next section (Section 3. machine learning) was verified using the real experimental data generated from the LPBF of 316L SS samples. A set of processing parameters that were close to those recommended by the manufacturer for 316L SS material was selected for the validation run in this study. The selected processing parameters are listed in Table 1.

Table 1 Laser powder bed fusion (LPBF) operational process parameters.

Processing Parameters	Value
Laser Power (W)	100
Laser Energy Density (J / mm^3)	59.59
Scanning Speed (mm/s)	600
Hatch Distance (µm)	85
Layer thickness (µm)	32.9

316L stainless steel powder was used for the LPBF. The powder was manufactured using gas atomization and supplied by Trumpf (Germany) with a size range of 20- 40 μm. The powder was characterized by a Gaussian- like particle size distribution. The particle diameter distribution values D10, D50, and D90 are 20.6 μm, 28.3 μm, and 39.5 μm, respectively [75].

2.1. LPBF Process

The 3D printed specimens were produced at room temperature and relative humidity of 50 ~ 70 % using a TruPrint 1000 LMF (TRUMPF, GmbH, Germany) with 200 W TRUMPF fiber laser system, laser wavelength of 1070 nm, standard beam diameter of 55 μm, layer thickness of 10 – 50 μm, build rate of 2 – 18 cm^3/h, standard minimum measurable oxygen level down to 3000 ppm, and the shielding gases Nitrogen and Argon. The system was equipped with an integrated high- resolution camera and an automatic image processing function for optimal powder bed process monitoring, which gives the option to a constant overview of the state of the component and investigate the quality parameters layer by layer. Argon was used to prevent excessive oxidation during the printing process; simultaneously, the oxygen level was kept constant to increase the quality of the parts.

The printing process started with filling the powder feed chamber, then the powder re-coater was used to coat the first layer of powder on the build plate (printing stage), and immediately after that the laser was applied to melt the powder layer selectively. Once the built plate is coated, the re-coater was used to dispose the excess powder into an overflow bin, then a new layer of powder was applied uniformly on the printed surface and the fabrication process continued for the new top powder layer until the part is completed. Three dog–bone shaped samples were separately printed with a gauge length cross-section of 3.1 mm × 5 mm and gauge length of 33.7 mm according to ASTM E8/E8M-11, as shown in Fig. 1(a) and Fig. 1(b) [76]. The alternating stripes laser scanning strategy has been conducted, where the scanning direction was changed 90° from the previous layer after the completion of each layer, as shown in Fig. 1(c). All samples were printed in the building direction along the Z axis, as indicated in Fig. 1(d).

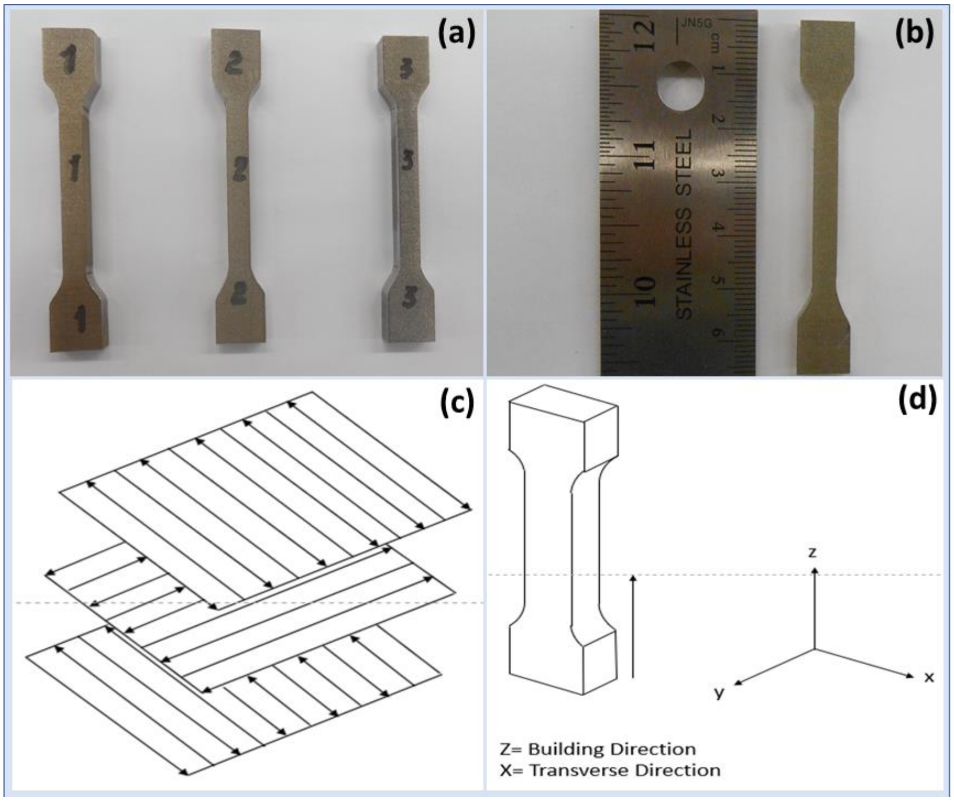

Fig. 1 (a) LPBF printed 3 dog-bone sample, (b) LPBF made sample with scale, (c) Schematic diagram of Printing Strategy by alternating scanning direction by 90, (d) Schematic diagram of build direction.

A few studies [3, 22, 29,77, 78, 87] show that besides the process parameters, the specimen building direction, shield gas circulation speed, and oxygen content may influence the final mechanical properties of SLM processed specimens. In the present study, only vertically built (direction) specimens are considered. It was due to the fact that the most of the available data in literature sources that could be used in this study were from the vertically built specimens. Therefore, to be consistent with the available data to be used for developing machine learning algorithm and model validation, specimens were built vertically for experimental examinations in this study.

2.2. Microstructure Analysis

The metallography samples were ground, polished, and etched prior to the microscopic observation. The etching was done using a solution consisting of HNO_3 (10 ml) and H_2O (30 ml) for 60 seconds, as recommended by ASTM E407-07 (2015) [79]. Zeiss Axiovert 40 MAT Optical Microscope (Focus Precision Instruments, Victoria, MN) and JEOL JSM-6490LV Scanning Electron Microscope (SEM) (JEOL Peabody, MA, USA) were used for microstructural investigations. Grain size and melt pool were measured using the linear intercept method according to ASTM E112-13 (2013) [80]. Density measurement was carried out using the hydrostatic balance principle according to ASTM B 311-17 [81].

2.3. Vickers Indentation

The hardness tests on the LPBF processed 316L SS samples were conducted using a Sun-Tec Hardness Testing machine under an applied load of 9.8 N for 12 seconds according to ASTM E E384-17 [82]. The measurements were performed in a plane parallel to the building direction (surface) as well as perpendicular to the building direction (cross section) of the LPBF printed 316L SS specimens. The results were obtained from the average of 10 indentations while maintaining a reasonable distance from each other to prevent work hardening effects.

2.4. Tensile Test

The uniaxial tensile tests were conducted using an Instron 8874 equipment that is a servo-hydraulic power drive machine equipped with a 250 kN load cell and a 20 Hz sampling frequency. The samples were printed with a dog bone shape according to the ASTM E8/E8M-11 where the gauge length of the sample was 33.7 mm, the thickness was 3.1 mm, and the width was 5 mm [76]. Tensile tests were carried out with a loading perpendicular to the laser printing tracks on three LPBF processed samples with a cross head speed of 2.5 mm/min.

3. MACHINE LEARNING

3.1. Machine Learning Implementation Algorithm

In the present study, we have tried several algorithms by providing input data (process parameters) and the output results (materials properties) were compared in terms of accuracy of predicted response variables. The machine learning method was implemented using a feedback loop system on six logically inter-linked steps, as shown in the flow-chart algorithm presented in Fig. 2.

Step 1. Data Collection. Experimental data from reliable literature reported on characterization of LPBF processed 316L SS samples were collected in this step. Experimental data from reliable literatures were tabulated and analyzed for consistency before use in this study. It was tried to mainly use data from vertically built specimens to increase consistency of the results. In conclusion, the experimental data from sixty-seven literature sources were taken into consideration for the present study. In addition, five process parameters, namely, laser power, laser energy density, scanning speed, hatching distance, and layer thickness were evaluated here. It is worth noting that machine type and material quality such as powder particle size and type can also influence on the final material properties. However, due to the limited availability of acceptable data they could not be examined in this study. Before applying machine learning models, all collected data are sorted and any missing data points were eliminated from the data set. Subsequently, all response data outliers also were removed completely from the data sets.

Step 2. Data Categorization. The collected data was sorted into two subsets: a) a numerical display format of input data predictors consisting of process parameters such as laser power, laser density, scanning speed, and hatching distance and b) output responses consisting of hardness, yield strength, ultimate tensile strength, and relative density.

Step 3. Data Division. The collected data was split into two sub-groups of model training data and model testing data (model validation data) using a uniform random data selection function.

Step 4. Model Selection and Implementation. In this step, the model type, machine learning algorithm, and its initial parameters were selected.

Step 5. Simulation. The selected machine learning algorithm with selected parameters was simulated with the training data set, and its performance was assessed, and its response prediction accuracy monitored, taking into account its missed/misclassified responses. This step was an iterative process run for a number of times (greater than 50) until the chosen model showed no more improvement in terms its accuracy coefficient of determination (R^2), root mean squared error (RMSE), mean absolute error (MAE), and accuracy in predicting the response values or accuracy reached greater than 85%. The values of R^2, RMSE, MAE, and accuracy were computed from the following equations (2-5):

$$R^2 = 1 - \sum_{i=1}^{n}(y_i - f_i)^2 \Big/ \sum_{i=1}^{n}(y_i - \bar{y}_i) \quad (2)$$

$$RMSE = \sqrt{\sum_{i=1}^{n}(y_i - f_i)^2/n} \quad (3)$$

$$MAE = \sum_{i=1}^{n}|y_i - f_i|/n \quad (4)$$

$$Accuracy = (n_{correct}/n) * 100\% \quad (5)$$

where y_i is the observed value, $\bar{y}_i$ is the mean of the observed data, f_i is the predicted value, $n_{correct}$ number of correctly classified data points, and n is the number of total observations. The final parameter values were stored and recorded to be optimized via an iterative process and k-fold validation. The Kullback-Leibler (KL) divergence criterion was employed for the selection of the improved model [83].

Step 6. Model Validation. The optimized parameter values from the machine learning developed model were saved and taken for a cross-validation check with the testing data subset from Step 3. All model performances, such as predicted response and categories, were analyzed, stored, and reported as results.

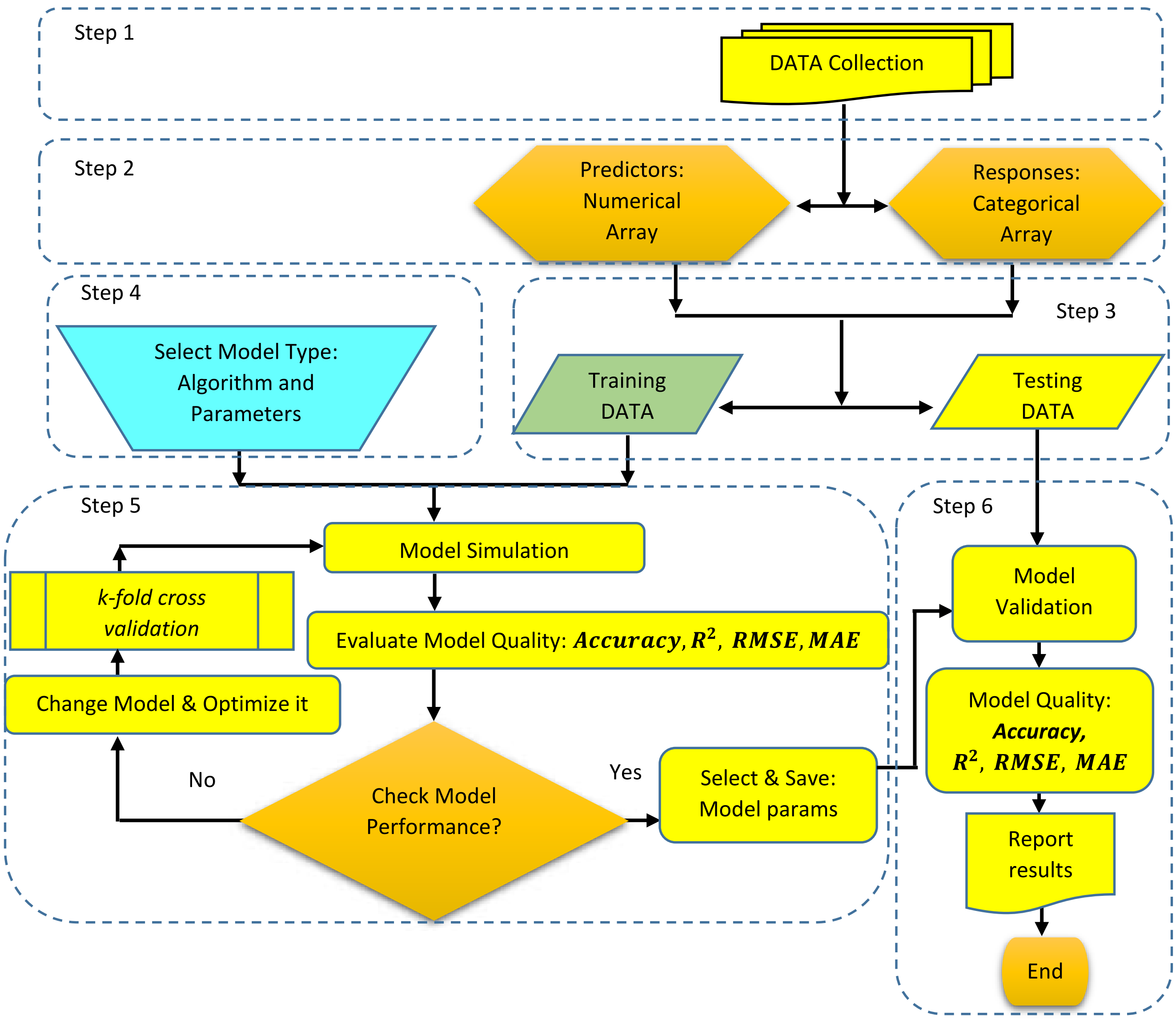

Fig. 2 Machine Learning model implementation algorithm.

3.2. Data Collection and Preparation

Operational process parameters and properties from 67 literature sources [5, 8-12, 14, 15, 17, 18, 19, 20-29, 31, 32, 38, 84- 126] on LPBF processed 316L SS samples were collected and verified in this study. As it is mentioned in "Step 1" of the previous section, all of the literature considered for the present analysis was specifically on the SLM processed 316L SS, since limited amount of reports are available on the application of machine learning on the process- property optimization of SLM processed 316L SS. In addition, it has been tried to select literatures that were consistent with respect to the reported properties. A wide range of process parameter values were also considered here to ensure that the present model globally covers the effect of processing parameters on the properties for a wide variation of material properties.

More than 170 data sets composed of the LPBF process parameters and the resulted mechanical properties of the samples were used as the input for machine learning process in this study. As it was mentioned in Section 1.1, the process parameters with a significant effect on properties of the final product in the LPBF process were identified as laser power in [*W*], laser energy density in [*J/mm^3*], scanning speed in [*mm/sec*], hatching distance [*mm*], and layer thickness [*mm*]. In addition to the density, mechanical properties such as ultimate tensile strength [*MPa*], yield strength [*MPa*], hardness [*HV*], and relative density [%] were also evaluated in this study.

The collected experimental data from the literature varied significantly. For instance, the data for process parameters were at following ranges; laser power = 50-450 [W], scanning speed = 60 - 3000 [mm/s], hatching distance = 0.02 - 0.1 [mm], layer thickness = 0.01-0.14 [mm], and Laser energy density = 19.35-1333 [J/mm^3]. The ranges of final properties of the specimens were: ultimate tensile strength = 178.37 - 751.6 [MPa], yield strength = 148.6- 643 [MPa], relative density = 59.83 - 100 [%], hardness = 163 - 281.3 [HV].

Data collection process: All collected data were preprocessed. There were couple of data points from each set of data, which were significant outliers which were removed. All data used in model training and validation were used without any adjustments or normalization. After removing the outliers, the data sets were split into two sub-sets of data – *model training* and *model validation* by selecting the data points using a uniform random number generator function. Table 2 shows a small sample of the sorted data set from the collected data from all the literature sources after initial deduction of overall collected data. After initial analysis, the sorted data were organized and categorized in the following order:

Predictors: LPBF process parameters: laser power, laser energy density, scanning speed, hatching distance, and layer thickness; columns 1 – 5.

Responses: Mechanical properties: yield strength, ultimate tensile strength, hardness, and relative density; columns 6 - 9.

Validation. Finally, to validate the accuracy of the implemented machine learning models, 316L SS samples were produced from a random set of predicted process parameters. Density and mechanical properties of printed samples were experimentally measured and compared to those predicted by the machine learning process in this study.

It is worth mentioning that almost all the literature referenced in this study have not reported all utilized process parameters (predictor data) used for the LPBF process in their studies, even though it applies to their investigation on physical mechanical properties (response data). Thus, Table 2 does not include the same number of data sets for all studied response variables. After the completion of sorting data in a tabulated format, the collected data were split into two data subsets: "training" and "testing." In general, approximately 70-80% of the collected data were used for training and 20-30% of the data were used for testing. The data selection process for training and testing was conducted using a uniform random distribution approach. Moreover, while preparing the data for model training and testing, the collected and sorted data of the process parameters (the predictor variables, namely, laser power, laser energy density, scanning speed, hatching distance and layer thickness) were analyzed using the principal component analysis (PCA) to identify the predictor with the highest statistical significance and correlation with other predictors.

Table 2 The data obtained from literature for training the model.

Ref	**Predictors:** LPBF process parameters					**Responses:** Mechanical properties			
	Laser Power (W)	**Laser energy Density, J/mm3**	**Scanning Speed, mm/s**	**Layer Thickness, mm**	**Hatch Distance, mm**	**YS_ Ver (MPa)**	**UTS_ Ver (MPa)**	**Hardness, HV**	**RD (%)**
[18]	90	20	1000	0.03	0.15	430.4±11	509.0±3.0	-	-
[29]	200	69.4	800	0.03	0.12	589.89±11.86	698.98±23.65	-	-
[05]	150	208.33	400	0.03	0.06	489.9±17.2	548.3±18.8	-	-
[96]	100	70	0.25	0.05	0.114	-	-	215.65±10.4	-
[124]	75	156	80	0.1	0.06	-	-	215±6	-
[112]	180	81.29	357	0.05	0.124				99.63±0.40
[116]	150	600	500	0.05	0.01				92.38±0.63
[5, 8-12, 14, 15, 17, 19, 20- 28, 31, 32, 38, 84-95, 97- 111, 113-115, 117-126]	…	…	…	…	…	…	…	…	…

3.3. Model Selection

Previously, it was explained that two types of models: (a) *supervised* and (b) *unsupervised,* were implemented by machine learning process and their performances were also compared in this study. The appropriateness of the implemented models was checked using the Kullback-Leibler (KL) divergence criterion [83], *k*-fold cross validation, R^2, RMSE, MAE, and accuracy. The KL divergence criterion measured the distances between the probability distribution of true values (data) and found fit model values [83]. Several distances, such as spearman, Minkowski, Euclidean, squared Euclidean, cosine, Chebyshev, city-block (Manhattan), and Mahalanobis distances, were taken into account and computed to cluster the predictor variable data. The KL criterion is commonly used in validating the appropriateness of a model [127]. The KL divergence between two models: (a) $f(X,\beta)$ and (b) $g(X,\mu)$, is defined by equation (6) [83, 127].

$$I(f,g) = \int f(X,\beta)\log([f(X,\beta)/g(X,\mu)])\,dX \tag{6}$$

where, $\boldsymbol{X}$ is predictor variables (independent variable), β is parameterization of the models $f(X,\beta)$, and μ is parameterization of the models $g(X,\mu)$. Note that in this case, $f(X,\beta)$ is the truth model (data), and $g(X,\mu)$ is the proposed model. The response (dependent) variable values Y are found from the regression model equations (7) and (8).

$$Y_1 = f(X,\beta) \tag{7}$$

$$Y_2 = g(X,\mu) \tag{8}$$

The computed KL divergence was used to compute the Akaike information criterion (AIC) [128] and Bayesian information criterion (BIC) criterion [129] modified version of AIC from equation (9) and (10), respectively.

$$AIC = 2K - 2\log[\mathcal{L}(\hat{\mu}|\mathrm{x})] \tag{9}$$

$$BIC = \log(n)K - 2\log[\mathcal{L}(\hat{\mu}|\mathrm{x})] \tag{10}$$

where K is the number of model parameters, n is the number of data points (or sample size), $\hat{\mu}$ is an estimated value of the best parameters found based on the lowest KL divergence criterion in $g(X,\mu)$, and x is the sample data (independent variable) of predictor variables. The performance of the *k*-fold cross validation process is shown in Fig. 3. The data is composed of predictors and responses. The initial predictors were process parameters, namely laser power (LP), laser energy density (LED), scanning speed

(SSpeed), and responses were the end properties of the LPBF processed parts, namely ultimate tensile strength (UTS), yield strength (YS), hardness (HV), and relative density (RD).

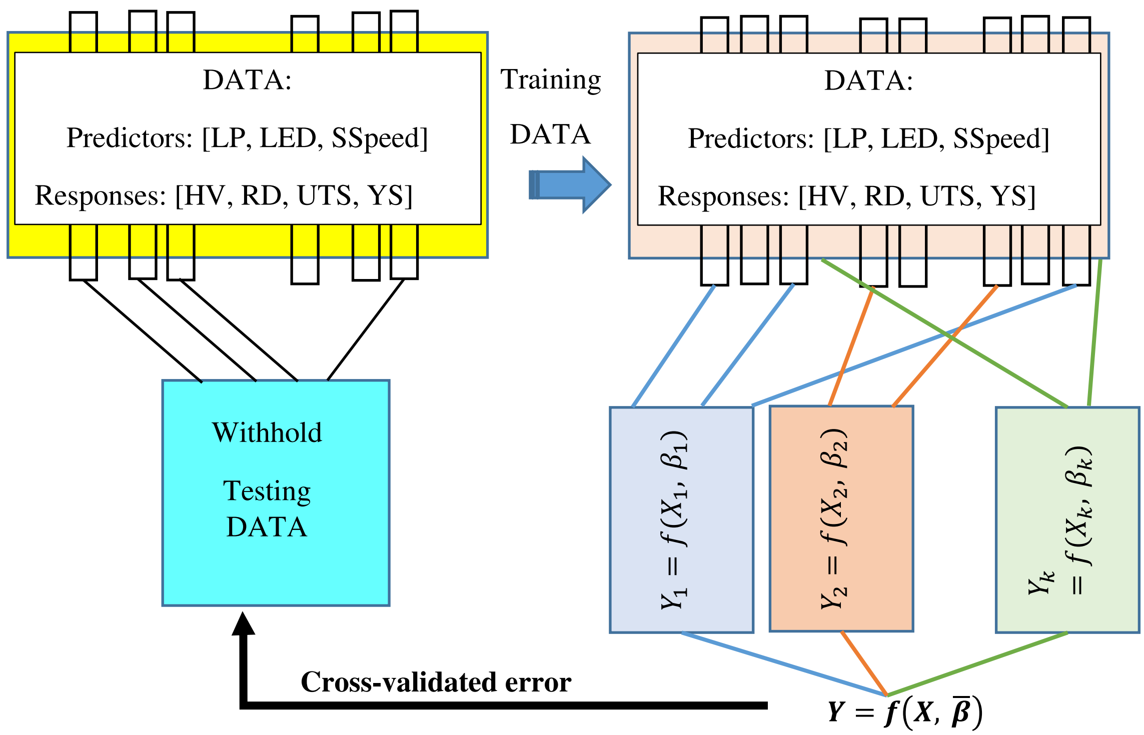

Fig. 3 Procedures of *k*-fold validation models [60].

3.4. Unsupervised Learning Models

One unsupervised learning algorithm – dendrogram clustering algorithm was implemented to study the accuracy of clustering the response variables of the collected data. A dendrogram is a simple hierarchical clustering algorithm [60] that is generated for either top-down or bottom-up approach. The following distance calculation methods between data points shown in equation (11 – 17) were taken in dendrogram and other supervised learning models [130-132].

$$Euclidean\ distance \quad \left\| x_j - x_k \right\|_2 \tag{11}$$

$$Squared\ Euclidean\ distance \quad \left\| x_j - x_k \right\|_2^2 \tag{12}$$

$$Minkowski\ distance \quad \sqrt[p]{\sum_{j=1,k=1}^{n} \left(x_j - x_k\right)^p} \tag{13}$$

$$City\ block\ (Manhattan)\ distance \quad \left\|x_j - x_k\right\|_1 \tag{14}$$

$$Chebyshev\ (Maximum)\ distance \quad \left\|x_j - x_k\right\|_\infty \tag{15}$$

$$Mahalanobis\ distance \quad \sqrt{\left(x_j - x_k\right)^T C^{-1}(x_j - x_k)} \tag{16}$$

$$Cosine\ distance \quad 1 - x_j x_k' / \sqrt{\left(x_j x_j'\right)\left(x_k x_k'\right)} \tag{17}$$

where x_j, x_k are predictor data points at j and k location, C^{-1} is the covariance matrix, and p power values. A special case values of p give the city-block ($p = 1$), Euclidean ($p = 2$), and Chebyshev ($p = \infty$) distances.

3.5. Supervised Learning Models

Three supervised learning models: (a) k-nearest neighbors (kNN), (b) ensemble learning decision tree, and (c) support vector machines (SVM) algorithms [133-136], were implemented in this study. The kNN, one of the commonly used machine learning algorithms, was implemented with optimized hyper parameters to classify the response variables using categorical and numerical arrays. The ensemble learning decision tree algorithm, composed of several decision tree models, was implemented with six different learner functions: (a) hyper parameter, (b) kNN, (c) tree, (d) linear discriminant, (e) single kNN template, and double kNN template. Finally, the SVM algorithm was implemented in five different model configurations, namely, (a) standardized predictor, (b) 5-fold cross validation, (c) Gaussian kernel function, (d) radial basis kernel function, and (e) polynomial kernel functions, to predict numerical values of the response variables based on regression. The implemented supervised learning models were trained and validated to classify and predict the response variables, namely, hardness in [*HV*], yield strength in [*MPa*], ultimate tensile strengths in [*MPa*], and relative density in [%] resulted from varying LPBF process parameter values according to pre-defined six categories (Grade A-F, see Table 3). In the developed machine learning models, the process parameters are taken as predictors, namely laser power in [*W*], laser energy density in [J/mm^3], scanning speed in [*mm/sec*], hatching distance in [*mm*], and layer thickness in [*mm*]. In addition, the distances between the data points were computed using equations (10-16), while performing data classification with these supervised models.

4. SIMULATION AND DATA ANALYSIS TOOLS

All developed machine learning models, algorithms, and simulations were carried out using MATLAB software [137] using its built-in functions, such as Statistics and Machine Learning Toolbox™ and data analysis tools [137-139].

4.1. Principal Component Analysis of Predictors

As mentioned before, the most effective process parameters that can influence additive manufacturing of metallic parts are laser power (LP), laser energy density (LED), scanning speed (SSpeed), layer thickness, and hatching distance (HD) [69, 71]. Moreover, the Equation (1) shows that LED is directly proportional to LP and inversely proportional to SSpeed, HD and layer thickness. The collected data from the literature sources show that many researchers specified LED values by incorporating the values of HD and layer thickness. Many other studies taken the same or similar values for HD and layer thickness. For instance, about half of the collected data from literature showed that they had used 0.03 mm of layer thickness, and 0.08 and 0.124 mm for HD. In order to find out the influence of all these five input parameters, the principal component analysis (PCA) of the prepared and arranged data of predictor variables was performed before starting simulations on the developed machine learning models. The principal components were computed and compared against the five process parameters as shown in Fig. 4. This graph demonstrates that the five process parameters are not equally important in terms of their statistical significance on prediction of the properties of the LPBF processed parts. The most important process parameters were laser power (LP) with over 80% of variation, a second important one found to be the laser energy density (LED) with about 10% of variation and similarly, the third important process parameter is the scanning speed (SSpeed) with about 8% of variation. The other two parameters, namely, layer thickness (Layer) and hatching distance (HD) were insignificant in predicting the properties of the LPBF processed parts. It must be noted that the statistical significance was found based on the collected experimental data rather than mathematical significance or calculation of LED, from other parameters. Moreover, the overall working principles of ML algorithms and routines are based purely on statistical analysis of the input and output data and they are not based on mathematical derivations or calculations. According to the results obtained from PCA, three input parameters, i.e. LP, LED and SSpeed, are considered for simulations in this study as shown in Fig. 4. Therefore, HD and layer thickness were not taken into the account for the model training and validation steps. In the next step, two types of common machine learning models, which are classification and regression, were trained and validated.

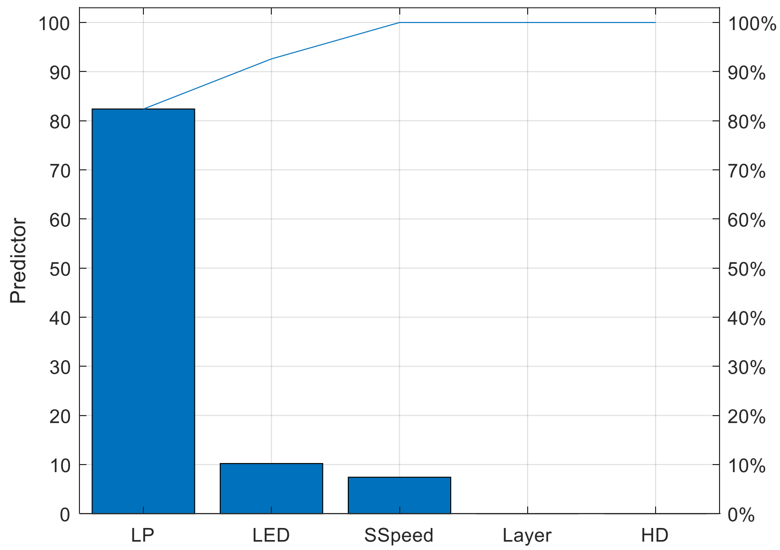

Fig. 4 Principal Component Analysis of Predictors.

4.2. Simulation of Classification Models

After sorting all collected data from the literature sources as shown in Table 2, missing data points and outliers are removed from the data sets. Then the processed data were clustered by employing unsupervised learning method to identify how many clusters (grade levels) of the response data, which are ultimate tensile strength, yield strength, hardness, and relative density. There were mostly two or three outlier points in response data. An example of application of an unsupervised learning algorithm with dendrograms is shown in Fig. 5 for the response data collected for ultimate tensile strength. The clustering simulation showed six clusters (six categories) of the response data of ultimate tensile strength using dendrogram analysis with "Euclidian" distance with 25 leaf nodes and 25% threshold values. The employed unsupervised learning (clustering approach) model to find out how many sub-groups to consider for classification purposes in the classification models. The reason for choosing 25 leaf nodes and resulted six clusters (Grade levels) was to make equal grids and symmetrical distribution of the response data (ultimate tensile strength, yield strength, hardness, and relative density) collected from the literature sources. The chosen 25 leaf nodes along y-axis in Fig. 5 show how indices of the data points laying in cluster (Grade A, B, C, D, E, F). The sub-clusters under Grade B is close to the ones in Grade C. Similarly, Grade D and E are also close to each other. On the other hand, the distance between Grade A is far from Grade B and C. The distance between Grade D and E are quite far from Grade F cluster elements. Similar dendrograms were obtained for yield strength, relative density, and hardness. Each cluster was defined to be one grade.

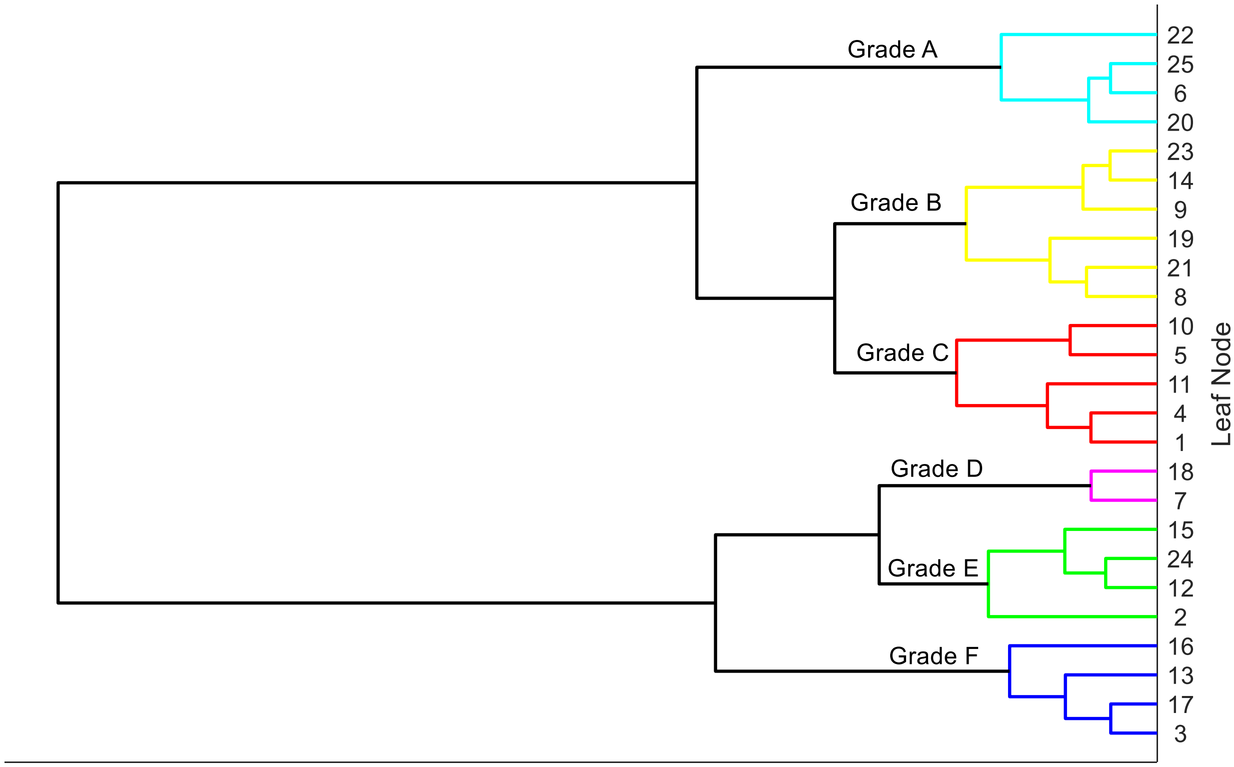

Fig. 5 Dendrograms of ultimate tensile strength data.

The classified six categories, such as Grade A – F in a descending order shown in Table 3. These categorized response data were used as a training and testing data sets in simulation of kNN classification model. The classification of the response variables (hardness, yield strength, ultimate tensile strength, and relative density) was conducted using the ranges of values as listed in Table 3.

Table 3 Created categories of the response data.

Category	Hardness, [*HV*]	Ultimate Tensile Strength, [*MPa*]	Yield Strength, [*MPa*]	Relative Density, [%]
Grade A	263.1 ± 10	704 ± 48	602± 41	96.5 ± 3.5
Grade B	243.1 ± 10	589 ± 48	558 ± 41	93 ± 3.5
Grade C	223.1 ± 10	522 ± 48	476 ± 41	87 ± 3.5
Grade D	213.1 ± 10	408 ± 48	394 ± 41	83.5 ± 3.5
Grade E	193.1 ± 10	293 ± 48	312 ± 41	77 ± 3.5
Grade F	173 ± 10	184 ± 48	148 ± 41	63.5 ± 3.5

The k-nearest neighbor (kNN) classification method is one of the simplest supervised learning algorithms that is easy to understand, implement, and execute [83]. The kNN classification algorithm was modeled, trained, and tested with a 10 - nearest number neighborhood and optimized hyper parameters of the kNN algorithm with the pre-separated training and testing data. The implemented kNN model using the optimized parameters reached 100% accuracy after several iterations with the training data, and these training data was composed of about 80% of the collected hardness data. All misclassified data sets from the initial iterations of a model training process were used again in the subsequent iterations. In measuring the distance between the classified data points and true values, Euclidian distance – Eq. (11) was employed. While optimizing kNN models, 5 to 10 data point k-fold values were used. The found best kNN model from the training data was validated with the remaining (20%) of the testing data. Fig. 6 shows the confusion chart of the classified (found) data of hardness with a 100% accuracy. The 100% accuracy was obtained after several iterations of model training. The accuracy shows how many predicted values of hardness match with true hardness values given in the source experimental data. The numbers, shown inside blue colored square cells along the diagonals (Fig. 6), are the number of correctly categorized data points. Classification (categories) of the predefined Grade value ranges are given in Table 3. As an example, the number 6 in cell 1 (Fig. 6) shows how many hardness data values lie within 173 ± 10 HV (Grade F), 12 shows that there are 12 hardness data points are within 193.1 ± 10 HV (Grade E), and similarly, 23 shows that there are 23 hardness values under category D. The grades in Fig. 6 shows along x-axis are predicted class, and the ones along y-axis are true class. The similar high accuracy was attained for the other data sets of ultimate tensile strength, yield strength, and relative density, and thus, the results are not shown here.

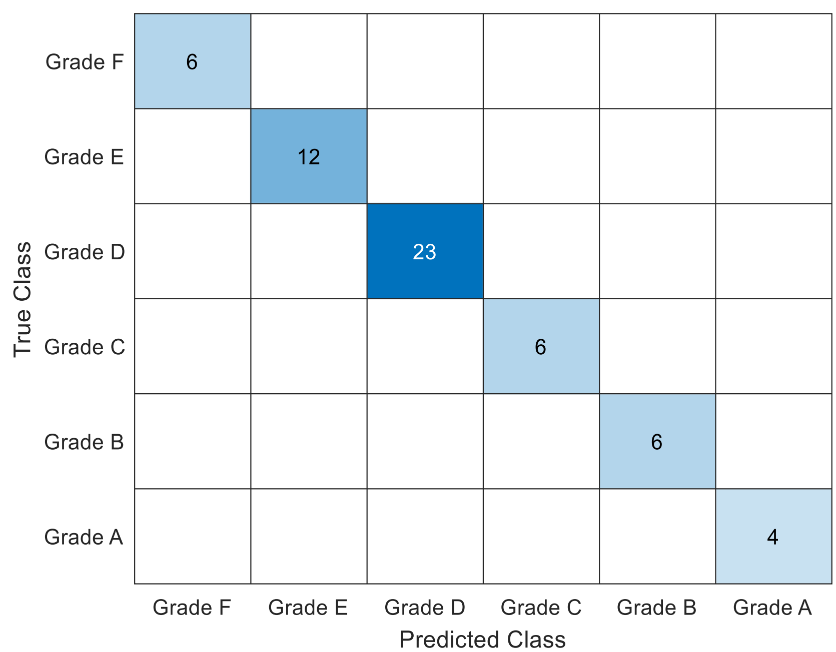

Fig. 6 Classification of response variable – hardness with respect to pre-defined six classifications as listed in Table 1.

The ensemble tree-based classification algorithm is one of the most powerful supervised learning algorithms of machine learning. During the ensemble tree-based classification algorithm, numerical (original) response data were directly used with no predefined classification (Grade A, B, …, F) similar to supervised learning models. Six different models of the ensemble tree algorithm were implemented, as listed in Table 4.

Table 4 Classification models of the ensemble tree-based algorithm.

Model type	Model parameters
Model 1. Hyper-Parameter Model	Optimized Hyper Parameters: [Learning Rate = 1, Method = Tree]
Model 2. kNN Model	Learner: kNN, [Euclidian Distance, kNN=1, Method = Classification, Learning Rate = 1, Method = Tree, N(trained) = 100]
Model 3. Tree Model	Learner: Tree, [Learning Rate = 1, Method = Tree, N(trained) = 100, N (nodes) = 21]
Model 4. Discriminant	Learner: Discriminant, [Learning Rate = 1, Method = Tree, N(trained) = 100, method = pseudolinear]
Model 5. Single kNN Template	Learner: kNN Template, [Method = Classification, Learning Rate = 1, Method = Tree, N(trained) = 100, Learning Template kNN = 5]
Model 6. Double kNN Template	Learner: kNN Template, [Method = classification, learning Rate = 1, Method = Tree, N(trained) = 200, Learning Template1 kNN = 3, Learning Template2 kNN = 9]

The prediction of relative density for LPBF processed 316L SS was conducted using total of 149 data points from variables extracted for laser power (LP), laser energy density (LED), scanning speed (SSpeed), and the response of relative density. 70% of the data points were used for training (i.e., 105 data points) and the rest were used for testing and validation (i.e., 44 data points). The simulation results shown in Fig. 7 and Table 5 indicated that Model 6 could predict density with accuracy greater than 86% with the smallest error (ERROR, MAE, RMSE) using collected data for LP, LED, and SSpeed.

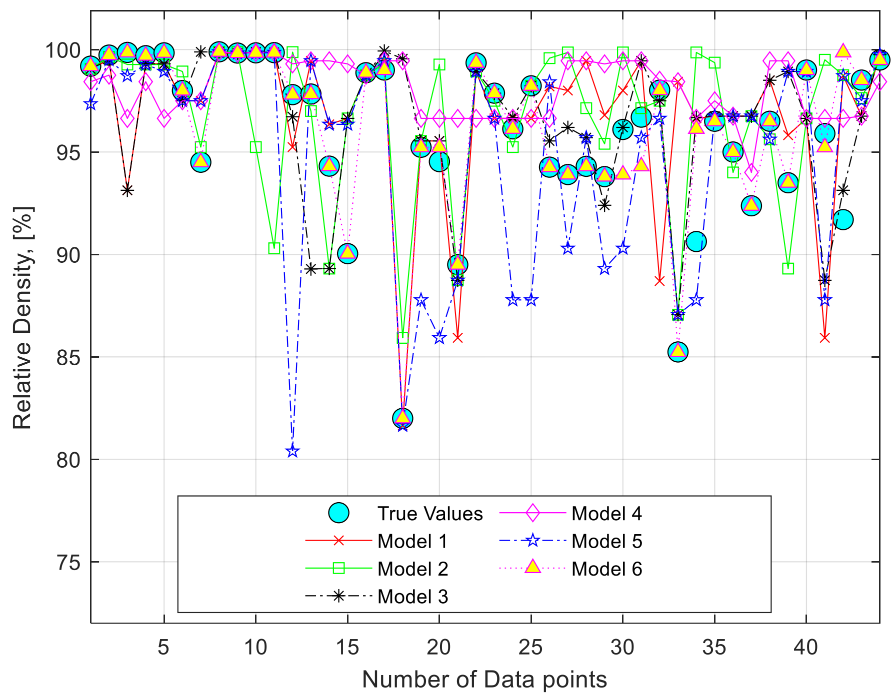

Fig. 7 Classification of the relative density of LPBF processed 316L SS samples using Ensemble tree-based classification algorithm with six different model configurations.

Table 5 Relative density prediction via classification models.

Assessment Parameter	Model 1	Model 2	Model 3	Model 4	Model 5	Model 6
Accuracy	~50%	~50%	~70%	~10%	~10	**~86%**
ERROR	0.1571	0.2571	0.1524	0.7524	0.2000	**0.1364**
MAE	1.8059	2.3348	2.3008	3.0388	2.8909	**0.4932**
RMSE	0.0276	3.4418	4.0033	4.6017	4.1117	**1.5156**
R^2	~0.95	~0.95	~0.95	~0.95	~0.99	**~0.99**

Fig. 8 and Table 6 present the same results from prediction of hardness for LPBF manufactured 316L SS samples using different machine learning models. Seventy percent of the data points were used for training (i.e., 58 data points) and the rest were used for testing and validation (i.e., 27 data points). Again, Model 6 demonstrated the highest accuracy (greater than 89%) and smallest error (ERROR, MAE, RMSE) in correctly predicting the response variable values based on the three predictors (LP, LED, and SSpeed).

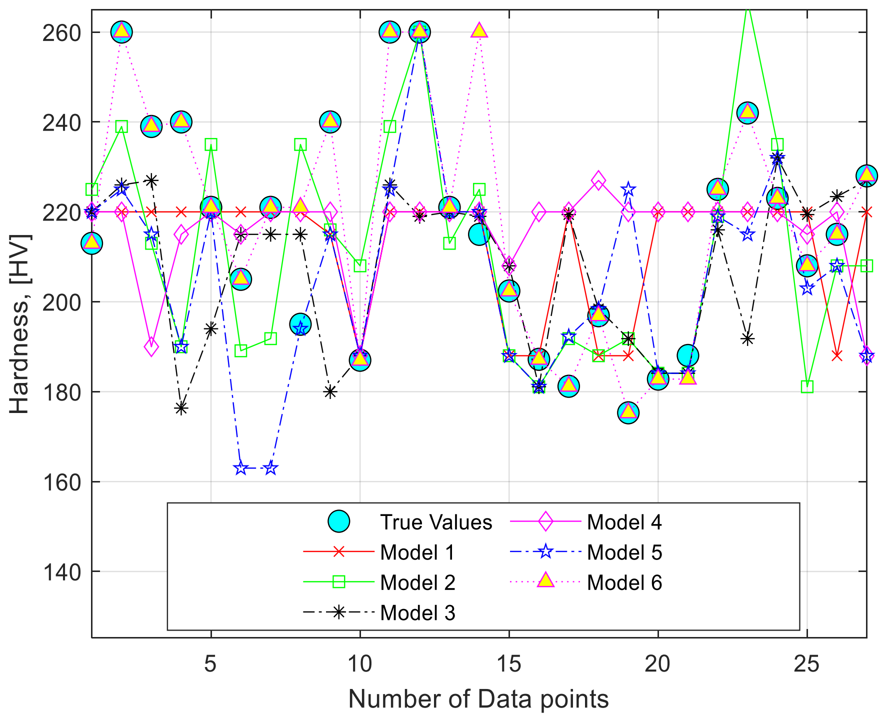

Fig. 8 Classification prediction of the hardness of LPBF processed 316L SS samples using Ensemble tree-based classification algorithm with six different model configurations.

Table 6 Hardness prediction via classification models.

Assessment parameter	Model 1	Model 2	Model 3	Model 4	Model 5	Model 6
Accuracy	~10%	~60%	~10%	~10%	~50%	**~89%**
ERR	0.8615	0.4308	0.2000	0.8308	0.3692	0.1111
MAE	17.1019	18.6704	17.8815	21.0426	17.1009	2.8241
RMSE	0.2188	25.8913	25.6930	26.6266	24.8690	10.0528
R^2	~0.95	~0.95	~0.95	~0.95	~0.99	**~0.99**

The simulation results for prediction of ultimate tensile strength of the LPBF 316L SS are tabulated in Table 7 and shown in Fig. 9. Seventy-five percent of the data points were used for training (i.e., 68 data points) and the rest were used for testing and validation (i.e., 26 data points). Model 6 was the one with the highest accuracy (greater than 89%) and smallest error (ERROR, MAE, RMSE).

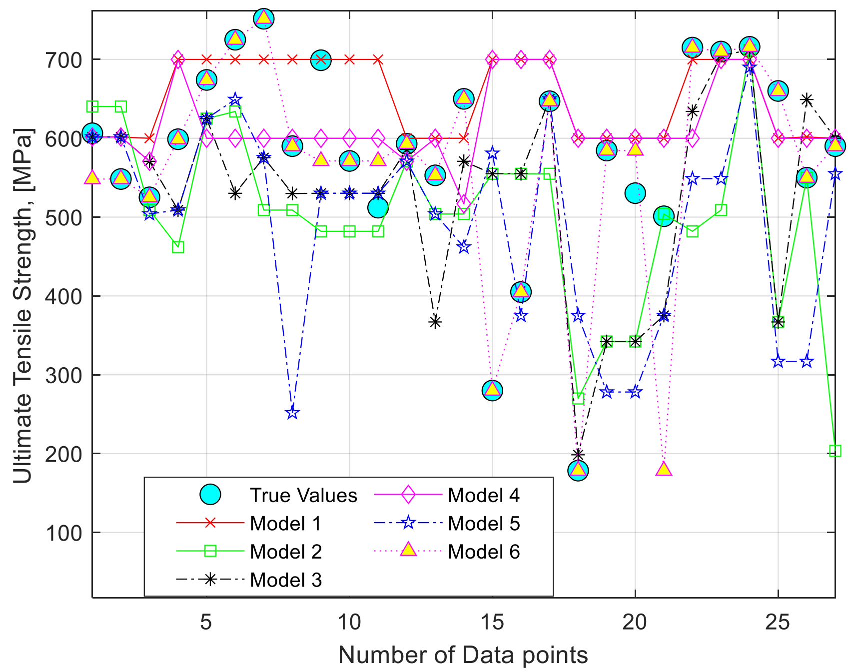

Fig. 9 Classification prediction of the ultimate tensile strength of LPBF processed 316L SS samples using Ensemble tree-based classification algorithm with six different model configurations.

Table 7 Ultimate tensile strength prediction via classification models

Assessment parameter	Model 1	Model 2	Model 3	Model 4	Model 5	Model 6
Accuracy	~10%	~60%	~10%	~10%	~50%	**~89%**
ERR	0.8615	0.4308	0.2000	0.8308	0.3692	**0.1111**
MAE	17.1019	18.6704	17.8815	21.0426	17.1009	**2.8241**
RMSE	0.2188	25.8913	25.6930	26.6266	24.8690	**10.0528**
R^2	~0.95	~0.95	~0.95	~0.95	~0.99	**~0.99**

Fig. 10 and Table 8 show the predictions of yield strength from collected data LP, LED, and SSpeed. 70% of the data points were used for training (i.e., 52 data points) and the rest were used for testing and validation (i.e., 21 data points). It should be noted that among all collected data sets from the literature, the number of reported data for the yield strength was significantly lower than the ones available for relative density, hardness, and ultimate tensile strength. The analysis of data using machine learning resulted in prediction of yield strength and Model 6 again demonstrated the highest accuracy (>85%) with smallest error margins (ERROR, MAE, RMSE). Table 9 shows the optimal process parameters found from the classification model 6 for the highest response variables. It is interesting to note that the optimized laser energy density values fall between the range of ~40- 150 J/mm^3, which was reported to be an optimized range for achieving superior properties for a SLM processed 316L SS [140- 142].

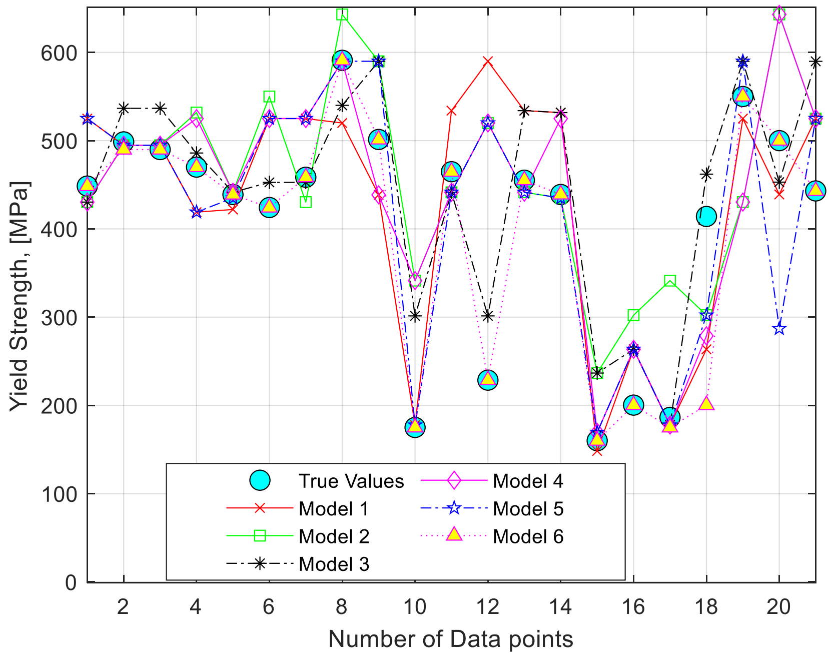

Fig. 10 Classification prediction of yield strength of LPBF processed 316L SS samples using Ensemble tree-based classification algorithm with six different model configurations.

Table 8 Yield strength prediction via classification models.

Assessment parameter	Model 1	Model 2	Model 3	Model 4	Model 5	Model 6
Accuracy	~10%	~10%	~10%	~30%	~30%	**~85%**
ERR	0.8615	0.4308	0.2000	0.8308	0.3692	**0.1111**
MAE	17.1019	18.6704	17.8815	21.0426	17.1009	**2.8241**
RMSE	0.2188	25.8913	25.6930	26.6266	24.8690	**10.0528**
R^2	~0.95	~0.95	~0.95	~0.95	~0.99	**~0.99**

Table 9 Optimal process parameters found via classification model 6 according to highest response variable values.

LP, [W]	SSpeed, [mm/s]	LED, [J/mm^3]	Ultimate Tensile Strength, [MPa]	
			Experimental	Model 6
195	1083	125.42	751.6	751.6
			Yield Strength, [MPa]	
			Experimental	Model 6
200	950	87.719	643	643
			Hardness, [HV]	
			Experimental	Model 6
160	1000	76.19	250	250
			Relative Density (%)	
			Experimental	Model 6
192	1000	91.4	100	100

Most appropriate parameter values of all classification models were found using a trial and error approach.

4.3. Application of SVM Models

Five different support vector machine (SVM) regression algorithm models, listed in Table 10, were also employed to predict the numerical values of the response variables, i.e., relative density, hardness, ultimate tensile strength, and yield strength of LPBF processed SS 316L.

Table 10 Different SVM algorithm models used in this study.

Model type	Model parameters
Model A. Standardized Predictor	Standardized Predictors, Solver: Sequential Minimal Optimization Algorithm [143]
Model B. 5-Fold Cross Validation Standardized Predictor Model	Standardized Predictors, 5-Fold Cross Validation, Solver: Standardized
Model C. Gaussian Kernel Function model	Kernel Function: Gaussian, Cross Validation Partition: 15, Solver: Standardized
Model D. RBF Kernel Function	Kernel Function: Radial Basis Function, Solver: Standardized
Model E. Polynomial Kernel Function	Kernel Function: Polynomial, Solver: L1 – Quadratic Programming (L1QP) [144]

The simulation from the application of five different types of SVM algorithm models to predict relative density of LPBF 316L SS samples are shown in Fig. 11 and Table 11. Model E demonstrated the highest accuracy ($R^2 = 0.98$) and smallest error margins (Error, MAE, RMSE).

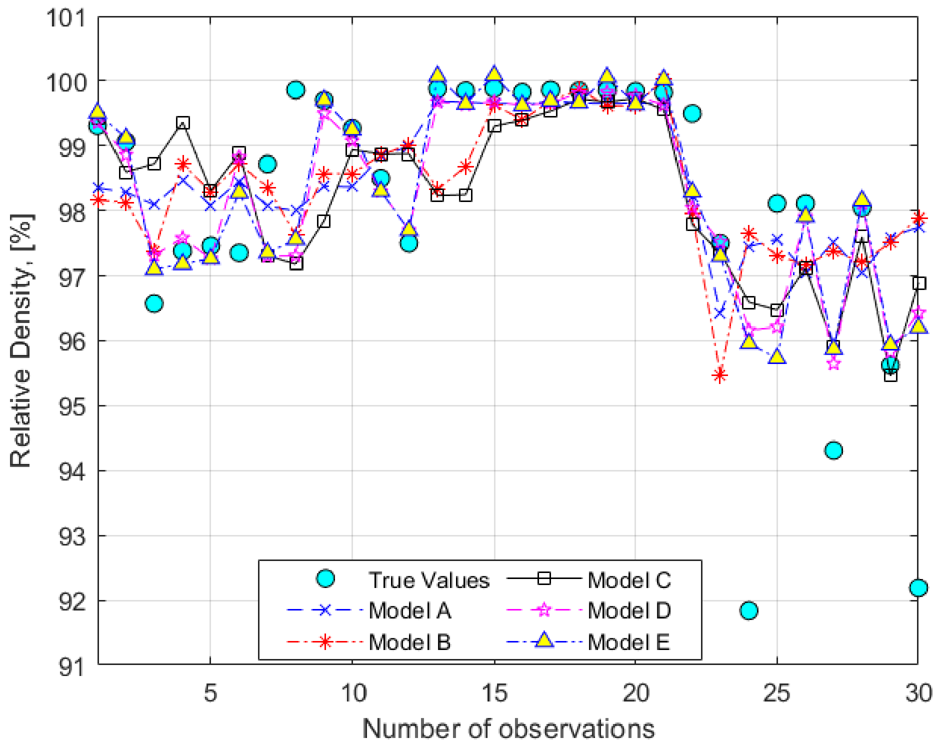

Fig. 11 Regression model prediction of relative density of LPBF processed 316L SS samples using SVM regression algorithm with five different models.

Table 11 Relative density prediction using regression models.

Assessment parameter	Model A	Model B	Model C	Model D	Model E
ERROR	3.6240	4.0814	3.5648	2.1569	**1.9973**
MAE	1.4374	1.5433	1.4136	0.9587	**0.9313**
RMSE	1.9037	2.0202	1.8881	1.4686	**1.4133**
R^2	~0.95	~0.95	~0.95	**~0.98**	**~0.98**

The hardness results obtained from application of SVM models indicated that Model C and E were capable of finding response values of hardness with highest accuracy ($R^2 = 0.99$) and smallest error margins (Error, MAE, RMSE), as shown in Fig. 12 and Table 12.

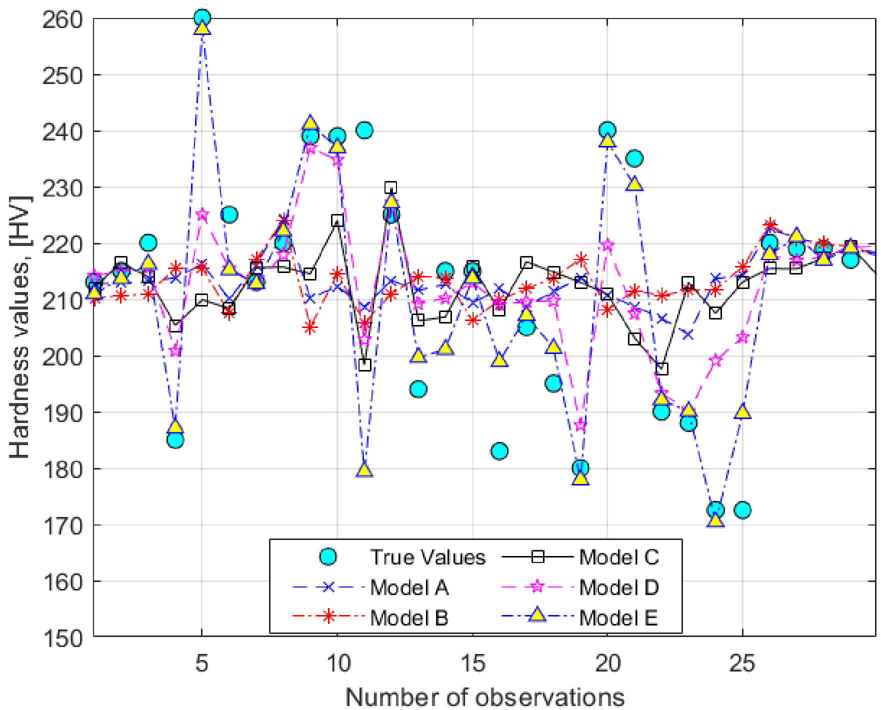

Fig. 12 Regression model prediction of Hardness values using SVM regression algorithm with five different models.

Table 12 HV prediction via regression models.

Assessment parameter	Model A	Model B	Model C	Model D	Model E
ERROR	337.8061	377.8964	307.5434	186.1893	**144.3593**
MAE	14.2539	15.3165	13.2390	9.3246	**6.8986**
RMSE	18.3795	19.4396	17.5369	13.6451	**12.0150**
R^2	~0.95	~0.95	~0.95	~0.98	**~0.99**

Five different types of SVM models were also used to predict the ultimate tensile strength of LPBF processed 316L SS using data sets for LP, LD, and SSpeed process parameters, and the results are shown in Fig. 13 and listed in Table 13. Here, both Model D and Model E predicted the ultimate tensile strength with high accuracy ($R^2 = 0.95$) and small error (Error, MAE, RMSE).

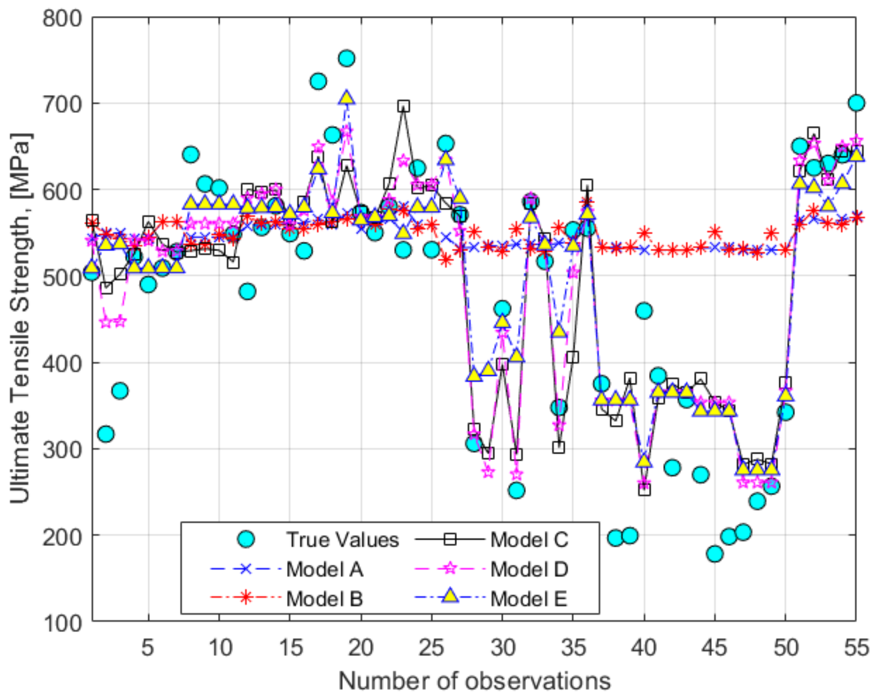

Fig. 13 Regression model prediction of ultimate tensile strength values using SVM regression algorithm with five different models.

Table 13 The ultimate tensile strength prediction via regression models.

Assessment parameter	Model A	Model B	Model C	Model D	Model E
ERROR	22917	23838	11772	**7238**	**7469**
MAE	151.3840	154.3970	108.4993	**85.0783**	**85.4227**
RMSE	113.6654	115.9051	78.8534	**58.2736**	**60.1108**
R^2	~0.92	~0.9	~0.95	**~0.95**	**~0.95**

SVM models were used to predict yield strength of LPBF manufactured 316L SS and the results are presented in Fig. 14 and Table 14. Again, Model D and Model E demonstrated highest accuracies ($R^2 = 0.95$) with the smallest error margins (Error, MAE, RMSE).

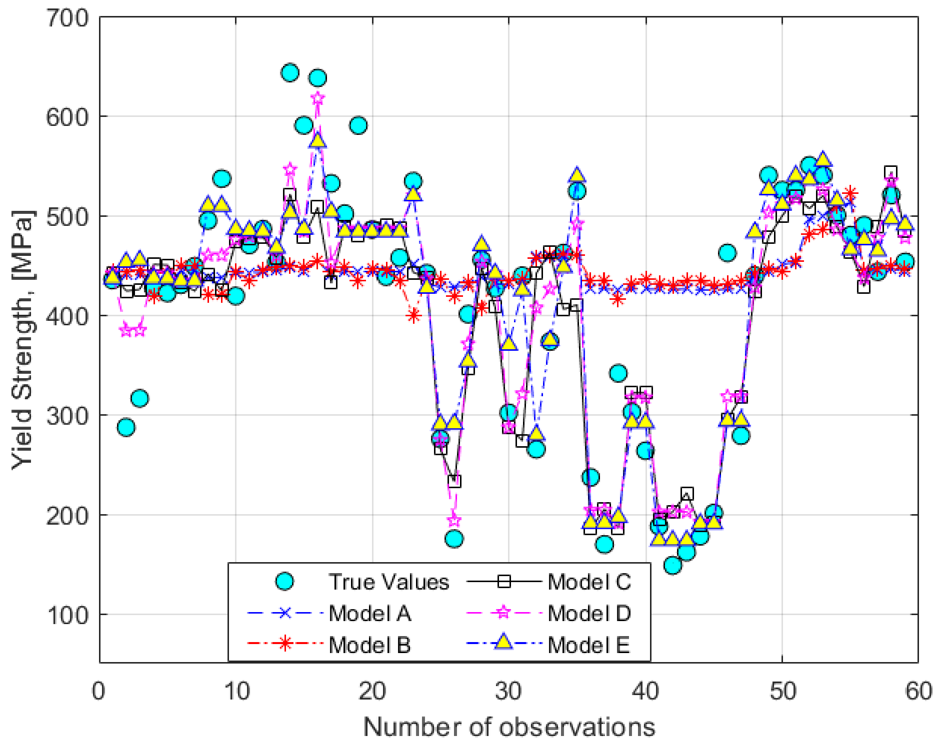

Fig. 14 Regression model prediction of yield strength values using SVM regression algorithm with five different models.

Table 14 The yield strength prediction via regression models.

Assessment parameter	Model A	Model B	Model C	Model D	Model E
ERROR	14709	15587	5127	**2878**	**3141**
MAE	89.2092	93.1940	53.1256	**37.7942**	**36.1886**
RMSE	113.6654	115.9051	78.8534	**58.2736**	**60.1108**
R^2	~0.92	~0.91	~0.95	**~0.95**	**~0.95**

Table 15 shows the optimal process parameters found from SVM regression Model E with respect to highest response variable values (ultimate tensile strength, yield strength, hardness, and relative density). According to SVM regression model E, the optimized laser energy density values fall between ~ 40-150 J/mm^3 of optimum value ranges reported in literature [140-142]. The present optimized laser energy density values also support the experimental observation where it was reported that SLM processed 316L SS had higher porosity content at laser energy density, which was lower or higher than the optimized range of ~40-150 J/mm^3 [140-142]. At lower laser energy, powder particles remained un-melted, and thus the porosity content became high. At higher laser energy density, excessive melting caused the formation of defects, such as keyholes, and thus the porosity content became high. Between the optimized range of ~40-

$150\,J/mm^3$, the porosity content was reported to be lowest, and thus highest relative density was achieved at this optimized range [140- 142].

Table 15 Optimal process parameters found via SVM regression Model E according to highest response variable values.

LP, [W]	SSpeed, [mm/s]	LED, [J/mm^3]	Ultimate Tensile Strength, [MPa]	
			Experimental	Model E
195	1083	125.42	751.6	704.3883
			Yield Strength, [MPa]	
			Experimental	Model E
195	1083	125.42	637.9	573.40
			Hardness, [HV]	
			Experimental	Model E
90	770.55	58.4	240	237.99
			Relative Density (%)	
			Experimental	Model E
380	1500	101.33	99.825	99.606

Most adequate parameter values of all SVM regression models were found using a trial and error approach.

4.4. Validation of the Models using Experimental Results

As it was indicated from the results, Model 6 of classification prediction algorithm (Section 4.2) and Model D and E of SVM regression algorithm (Section 4.3) of machine learning provided results with highest accuracy using data from literature for model training and testing. To validate the accuracy of these models in real conditions, a set of random process parameters was selected to print several samples using LPBF technology in this study. Mechanical and physical properties of LPBF processed samples were measured experimentally and compared to the ones predicted using the optimum machine learning algorithm (Model 6 of classification algorithm and Model D and E of SVM regression algorithm) in this study. The details of experimental procedure have previously explained in Section 2.

Fig. 15 (a) illustrates an etched cross section of LPBF processed 316L SS sample, which was observed in this study. The typical microstructure of a 3D printed metallic material containing semi-circular melt pools was clearly observed in this optical micrograph. The melt pools shown in Fig. 15 (a) formed in parallel to the printing direction, as indicated earlier in Fig 1 (d). These overlapped microstructural features (melt pools) indicated solidification of a high-density material resulting from the LPBF process. In Fig. 15 (b), an SEM micrograph showed an indentation on the un-etched cross section of the 316L SS sample produced in this study. A typical ductile deformation due to loading during indentation test was observed in this micrograph.

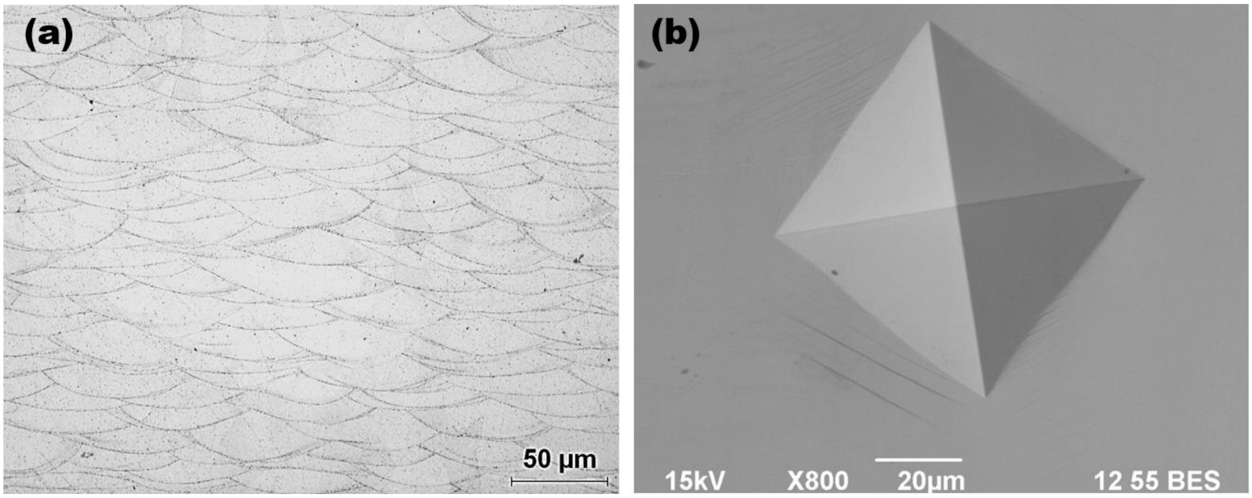

Fig. 15 (a) Optical micrograph of an etched cross section, and (b) SEM image of a Vickers indent on an un-etched cross section of LPBF processed 316L SS sample in this study.

Three Stress-strain curves resulted from tensile tests on the 316L samples produced by LPBF technology in this study are presented in Fig. 16. Important tensile properties, such as elastic modulus, yield strength, and ultimate tensile strength were obtained for 316L SS samples. Note that the elastic modulus was not used in this study due to the limited number of available literatures.

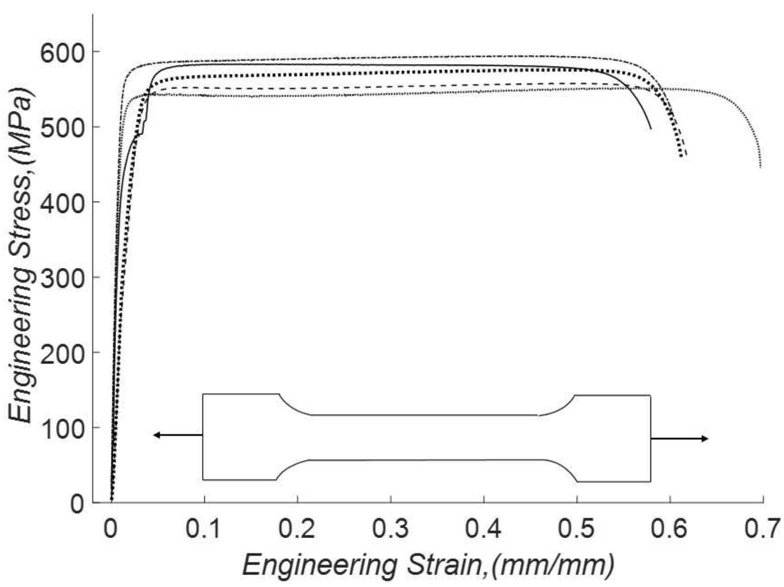

Fig. 16 Experimental stress- strain curve resulted from tensile tests on LPBF made 316L SS.

The experimentally measured density, hardness, and tensile property of the LPBF processed 316L SS samples are listed in Table 16 along with those calculated from Model 6 of classification algorithm and Model D and E of SVM regression algorithm.

Table 16 Comparison of density, hardness, yield strength, and ultimate tensile property of LPBF processed 316L SS with the predicted values from the application of optimum machine learning models in this study.

Properties	Measured Value	Predicted Value: (Classification) Model 6	Predicted Value: (SVM-Regression) Model D or E
Relative Density (%)	98.98	98.98	96.31 (96.66)
Hardness (HV)	221.04 ±8.91	220.00	221.30 (211.46)
Yield Strength (MPa)	515±50	439.00	515.31 (511.90)
Ultimate Tensile Strength (MPa)	573.82±17.45	573.30	588.59 (556.40)

Model 6 of classification prediction algorithm demonstrated about 99% accuracy in determining relative density, hardness, and ultimate tensile strength; however, it was less accurate in determining the yield strength. Similarly, the accuracy of the SVM regression algorithm models—Model D and E—was greater than 98% accurate in determining the resulted values of hardness, yield strength, ultimate tensile strength, and relative density. The relatively lower accuracy in determining the resulting yield strength with the classification model can be attributed to availability of smaller number of reported data sets in literatures for the yield strength, which could affect the training process and consequently reduced the accuracy of the model. It is indicated from the performed simulations and validation studies in this study that one classification algorithm-based model and two SVM regression algorithm models were found to be highly accurate in determining the end response values (relative density, hardness, yield strength, and ultimate tensile strength) of LPBF processed 316L SS samples. These highly accurate machine learning models, whose optimized parameter values were found via iterative simulations, demonstrated that they could work well with under 100 data samples. It is a very promising result for application of machine learning in characterization of properties of samples produced by an advanced additive manufacturing technology.

5. CONCLUSION AND RECOMMENDATIONS

Over 170 sets of experimental data for LPBF processed 316L SS samples were collected from 67 literature sources and analyzed using unsupervised and supervised machine learning algorithms. The collected data were divided into predictor and response types of data sets. The predictor variables were the LPBF process parameters, such as laser power, laser energy density, scanning speed, layer thickness, and hatching distance. The performed principal component analysis of the collected predictor data sets showed that only three out of the five predictors had a statistical significance. These are laser power, laser energy density, and scanning speed, which were implemented to both unsupervised and supervised machine learning algorithms. The response values, which are the mechanical properties of LPBF manufactured 316L SS, were predicted and classified by these three predictors. Six different classification models of the ensemble classification tree algorithm were also implemented in this study. The model with double kNN learning template with three and nine nearest neighbor data points showed consistently high accuracy (greater than 85%) for all simulated data sets of response and predictor data in predicting the response values according to the three predictors, which are LPBF process parameter values.

This study also examined application of five different support vector machine (SVM) regression models of supervised learning algorithms by machine learning to predict the end relative density, hardness, yield strength, and ultimate tensile strength of the LPBF processed 316L samples. Two of the applied SVM models with radial basis and polynomial kernel functions performed highest accuracy with smallest error (deviation), RMSE, MAE, and highest R^2 ranging from 0.95 to 0.99. Moreover, the validation studies with the experimental data demonstrated that the optimal SVM models (Model D and E) were highly accurate in predicting the mechanical properties of the 3D printed samples. To validate the result obtained from application of machine learning in this study, several of 316L SS samples were manufactured using LPBF technology. A random set of process parameters was selected to manufacture 316L SS samples. A series of experimental tests were performed to measure density, hardness, and tensile properties of the LPBF processed samples. The experimentally measured properties were very close to the ones predicted by the optimum classification and regression machine learning algorithm models in this study. The simulations of the implemented machine learning models using a large number of data collected from the literature resulted in the high accuracy prediction of characteristics of 3D printed metallic parts, which has not been previously reported in literature. Finally, this study demonstrates that three different machine learning models (one based on classification algorithm and two based on SVM regression algorithm) are found to predict mechanical characteristics of 3D printed 316L SS samples with high accuracy under 100 data points.

While results from this study are very promising, the capability of this technique to be applied as an industrial tool needs to be examined in more detail in future. In addition, the accuracy of the machine learning models can be improved not only with a large number of training data sets, but also with more predictor features. Therefore, future studies will be dedicated to study the influence of the LPBF process parameters on the micro-structure and cross-property connections using machine learning algorithms along with artificial neural networks in connection with application of image processing analysis.

Credit authorship contribution statement

Sulaymon Eshkabilov: Methodology, Validation, Formal analysis, Investigation, Writing – original draft. **Ismat Ara:** Validation, Formal analysis, Investigation. **Fardad Azarmi:** Investigation, Writing – review & editing, Supervision. **Igor Sevostianov:** Conceptualization.

DECLARATIONS

Funding

No external funding was used for this study.

Declaration of Completing Interest

The authors declare that they do not have any known competing financial interests or personal relationships that could influence the work reported in this paper.

Availability of data

All collected data used in this study is available.

Code Availability

MATLAB Codes will be provided only upon personal request.

Ethics Approval

Not Applicable.

Consent to Participate

Not Applicable.

Consent for Publication

Yes.

Acknowledgement

In loving memory of professor Igor Sevostianov.

REFERENCES

1. Hamza HM, Deen KM, Khaliq A, Asselin E, Haider W (2021) Microstructural, corrosion and mechanical properties of additively manufactured alloys: a review. Crit Rev Solid State Mater Sci: 1–53. https://doi.org/10.1080/10408436.2021.1886044.

2. Fayazfar H, Salarian M, Rogalsky A, Sarker D, Russo P, Paserin V, Toyserkani E (2018) A critical review of powder-based additive manufacturing of ferrous alloys: Process parameters, microstructure and mechanical properties. Mater Des 144: 98–128. https://doi.org/10.1016/j.matdes.2018.02.018.

3. Kok Y, Tan XP, Wang P, Nai MLS, Loh NH, Liu E, Tor SB (2018) Anisotropy and heterogeneity of microstructure and mechanical properties in metal additive manufacturing: A critical review. Mater Des 139:565–586. https://doi.org/10.1016/j.matdes.2017.11.021.

4. Gao W, Zhang Y, Ramanujan D, Ramani K, Chen Y, Williams CB, Wang CCL, Shin YC, Zhang S, Zavattieri PD (2015) The status, challenges, and future of additive manufacturing in engineering. Comput Aided Des 69: 65–89. https://doi.org/10.1016/j.cad.2015.04.001.

5. Gu D, Chen H (2018) Selective laser melting of high strength and toughness stainless steel parts: The roles of laser hatch style and part placement strategy. Mater Sci Eng: A. 725: 419–427. https://doi.org/https://doi.org/10.1016/j.msea.2018.04.046.

6. Kruth J, Mercelis P, Vaerenbergh J van, Froyen L, Rombouts M (2005) Binding mechanisms in selective laser sintering and selective laser melting. Rapid Prototyp J 11: 26–36. https://doi.org/10.1108/13552540510573365.

7. Chua CK, Wong CH, Yeong WY (2017) Standards, quality control, and measurement sciences in 3D printing and additive manufacturing. Academic Press.

8. Gong H, Snelling D, Kardel K, Carrano A (2019) Comparison of Stainless Steel 316L Parts Made by FDM- and SLM-Based Additive Manufacturing Processes. JOM. 71: 880–885. https://doi.org/10.1007/s11837-018-3207-3.

9. Chao Q, Thomas S, Birbilis N, Cizek P, Hodgson PD, Fabijanic D (2021) The effect of post-processing heat treatment on the microstructure, residual stress and mechanical properties of selective laser melted 316L stainless steel. Mater Sci Eng: A. 821: e141611. https://doi.org/10.1016/j.msea.2021.141611.

10. Kong D, Dong C, Ni X, Zhang L, Yao J, Man C, Cheng X, Xiao K, Li X (2019) Mechanical properties and corrosion behavior of selective laser melted 316L stainless steel after different heat treatment processes. J Mater Sci Technol 35: 1499–1507. https://doi.org/10.1016/j.jmst.2019.03.003.

11. Afkhami S, Dabiri M, Piili H, Björk T (2021) Effects of manufacturing parameters and mechanical post-processing on stainless steel 316L processed by laser powder bed fusion. Mater Sci Eng: A. e140660. https://doi.org/10.1016/j.msea.2020.140660.

12. Kong D, Ni X, Dong C, Lei X, Zhang L, Man C, Yao J, Cheng X, Li X (2018) Bio-functional and anti-corrosive 3D printing 316L stainless steel fabricated by selective laser melting. Mater Des 152: 88–101. https://doi.org/10.1016/j.matdes.2018.04.058.

13. Lou X, Othon MA, Rebak RB. Corrosion fatigue crack growth of laser additively-manufactured 316L stainless steel in high temperature water. Corros Sci 2017; 127: 120–130. https://doi.org/10.1016/j.corsci.2017.08.023.

14. Wang Y, Wang Y, Li R, Niu P, Wang M, Yuan T, Li K (2021) Hall-Petch relationship in selective laser melting additively manufactured metals: using grain or cell size? J Cent South Univ 28: 1043–1057. https://doi.org/10.1007/s11771-021-4678-x.

15. Ni X, Kong D, Wu W, Zhang L, Dong C, He B, Lu L, Wu K, Zhu D (2018) Corrosion Behavior of 316L Stainless Steel Fabricated by Selective Laser Melting Under Different Scanning Speeds. J Mater Eng Perform 27: 3667–3677. https://doi.org/10.1007/s11665-018-3446-z.

16. Choi JP, Shin GH, Brochu M, Kim YJ, Yang SS, Kim KT, Yang DY, Lee CW, Yu JH (2016) Densification Behavior of 316L Stainless Steel Parts Fabricated by Selective Laser Melting by Variation in Laser Energy Density. Mater Trans 57: 1952–1959. https://doi.org/10.2320/matertrans.M2016284.

17. Shin WS, Son B, Song W, Sohn H, Jang H, Kim YJ, Park C (2021) Heat treatment effect on the microstructure, mechanical properties, and wear behaviors of stainless steel 316L prepared via selective laser melting. Mater Sci Eng: A. 806: 140805. https://doi.org/10.1016/j.msea.2021.140805.

18. Suryawanshi J, Prashanth KG, Ramamurty U (2017) Mechanical behavior of selective laser melted 316L stainless steel. Mater Sci Eng: A. 696: 113–121. https://doi.org/10.1016/j.msea.2017.04.058.

19. Mertens A, Reginster S, Paydas H, Contrepois Q, Dormal T, Lemaire O, Lecomte-Beckers J (2014) Mechanical properties of alloy Ti–6Al–4V and of stainless steel 316L processed by selective laser melting: influence of out-of-equilibrium microstructures. Powder Metall 57: 184–189. https://doi.org/10.1179/1743290114Y.0000000092.

20. Carlton HD, Haboub A, Gallegos GF, Parkinson DY, MacDowell AA (2016) Damage evolution and failure mechanisms in additively manufactured stainless steel. Mater Sci Eng: A. 651: 406–414. https://doi.org/10.1016/j.msea.2015.10.073.

21. Yang Y, Zhu Y, Khonsari MM, Yang H (2019) Wear anisotropy of selective laser melted 316L stainless steel. Wear. 428: 376–386. https://doi.org/10.1016/j.wear.2019.04.001

22. Deev AA, Kuznetcov PA, Petrov SN (2016) Anisotropy of Mechanical Properties and its Correlation with the Structure of the Stainless Steel 316L Produced by the SLM Method. Phys Procedia 83: 789–796. https://doi.org/10.1016/j.phpro.2016.08.081.

23. Röttger A, Boes J, Theisen W, Thiele M, Esen C, Edelmann A, Hellmann R (2020) Microstructure and mechanical properties of 316L austenitic stainless steel processed by different SLM devices. Int J Adv Manuf Technol 108: 769–783. https://doi.org/10.1007/s00170-020-05371-1.

24. Lu P, Cheng-Lin Z, Hai-Yi L, Liang W, Tong L (2020) A new two-step selective laser remelting of 316L stainless steel: process, density, surface roughness, mechanical properties, microstructure. Mater Res Express 7: e056503. https://doi.org/10.1088/2053-1591/ab8b86.

25. Tucho WM, Lysne VH, Austbø H, Sjolyst-Kverneland A, Hansen V (2018) Investigation of effects of process parameters on microstructure and hardness of SLM manufactured SS316L. J Alloys Compd 740: 910–925. https://doi.org/10.1016/j.jallcom.2018.01.098.

26. Cherry JA, Davies HM, Mehmood S, Lavery NP, Brown SGR, Sienz J (2015) Investigation into the effect of process parameters on microstructural and physical properties of 316L stainless steel parts by selective laser melting. Int J Adv Manuf Technol 76: 869–879. https://doi.org/10.1007/s00170-014-6297-2.

27. Wang D, Song C, Yang Y, Bai Y (2016) Investigation of crystal growth mechanism during selective laser melting and mechanical property characterization of 316L stainless steel parts. Mater Des 100: 291–299. https://doi.org/10.1016/j.matdes.2016.03.111.

28. Tolosa I, Garciandía F, Zubiri F, Zapirain F, Esnaola A. (2010) Study of mechanical properties of AISI 316 stainless steel processed by "selective laser melting", following different manufacturing strategies. The Int J Adv Manuf Technol 51: 639–647. https://doi.org/10.1007/s00170-010-2631-5.

29. Hitzler L, Hirsch J, Heine B, Merkel M, Hall W (2017) Öchsner A. On the Anisotropic Mechanical Properties of Selective Laser-Melted Stainless Steel. Materials 10: e1136. https://doi.org/10.3390/ma10101136.

30. Meier H, Haberland CH (2008) Experimental studies on selective laser melting of metallic parts. Materwiss Werksttech 39: 665–670. https://doi.org/10.1002/mawe.200800327.

31. Spierings AB, Levy G (2009) Comparison of density of stainless steel 316L parts produced with selective laser melting using different powder grades. In: Proc. - 26th Annu Int Solid Free Fabr Symp - an Addit Manuf Conf SFF, pp 342-353.

32. Chen L, Richter B, Zhang X, Bertsch KB, Thoma DJ, Pfefferkorn FE (2021) Effect of laser polishing on the microstructure and mechanical properties of stainless steel 316L fabricated by laser powder bed fusion. Mater Sci Eng: A 802: e140579. https://doi.org/10.1016/j.msea.2020.140579.

33. Enneti RK, RMorgan R, Atre SV (2018) Effect of process parameters on the Selective Laser Melting (LPBF) of tungsten. Int J Refract Met Hard Mater 71: 315–319. https://doi.org/10.1016/j.ijrmhm.2017.11.035.

34. Liverani E, Toschi S, Ceschini L, Fortunato A (2017) Effect of selective laser melting (SLM) process parameters on microstructure and mechanical properties of 316L austenitic stainless steel. J Mater Process Technol 249: 255–263. https://doi.org/10.1016/j.jmatprotec.2017.05.042.

35. de Souza AF, Al-Rubaie KS, Marques S, Zluhan B, Santos EC (2019) Effect of laser speed, layer thickness, and part position on the mechanical properties of maraging 300 parts manufactured by selective laser melting. Mater Sci Eng: A 767: e138425. https://doi.org/10.1016/j.msea.2019.138425.

36. Nguyen QB, Luu DN, Nai SML, Zhu Z, Chen Z, Wei J (2018) The role of powder layer thickness on the quality of SLM printed parts. Arch Civ Mech Eng 18: 948–955. https://doi.org/10.1016/j.acme.2018.01.015.

37. Delgado J, Ciurana J, Rodríguez CA (2012) Influence of process parameters on part quality and mechanical properties for DMLS and SLM with iron-based materials. Int J Adv Manuf Technol 60: 601–610. https://doi.org/10.1007/s00170-011-3643-5.

38. Ahmadi A, Mirzaeifar R, Moghaddam NS, Turabi AS, Karaca HE, Elahinia M (2016) Effect of manufacturing parameters on mechanical properties of 316L stainless steel parts fabricated by selective laser melting: A computational framework. Mater Des 112: 328–338. https://doi.org/10.1016/j.matdes.2016.09.043.

39. Dong Z, Liu Y, Wen W, Ge J, Liang J (2018) Effect of Hatch Spacing on Melt Pool and As-built Quality During Selective Laser Melting of Stainless Steel: Modeling and Experimental Approaches. Materials 12: e12010050. https://doi.org/10.3390/ma12010050.

40. Lu Y, Gan Y, Lin J, Guo S, Wu S (2017) Lin J. Effect of laser speeds on the mechanical property and corrosion resistance of CoCrW alloy fabricated by SLM. Rapid Prototyp J 23: 28–33. https://doi.org/10.1108/RPJ-07-2015-0085.

41. DebRoy T, Mukherjee T, Wei HL, Elmer JW, Milewski JO (2021) Metallurgy, mechanistic models and machine learning in metal printing. Nat Rev Mater 6: 48–68. https://doi.org/10.1038/s41578-020-00236-1.

42. Majeed M, Khan HM, Rasheed I (2019) Finite element analysis of melt pool thermal characteristics with passing laser in SLM process. Optik. 194: e163068. https://doi.org/10.1016/j.ijleo.2019.163068.

43. Khan K, De A (2019) Modelling of selective laser melting process with adaptive remeshing. Sci Technol Weld Join 24: 391–400. https://doi.org/10.1080/13621718.2019.1575057.

44. Huang Y, Ansari M, Asgari H, Farshidianfar MH, Sarker D, Khamesee MB, Toyserkani E (2019) Rapid prediction of real-time thermal characteristics, solidification parameters, and microstructure in laser directed energy deposition (powder-fed additive manufacturing). J Mater Process Technol 274: e116286. https://doi.org/10.1016/j.jmatprotec.2019.116286

45. Mukherjee T, Wei HL, De A, DebRoy T (2018) Heat and fluid flow in additive manufacturing—Part I: Modeling of powder bed fusion. Comput Mater Sci 150: 304–313. https://doi.org/10.1016/j.commatsci.2018.04.022

46. Mukherjee T, Wei HL, De A, DebRoy T (2018) Heat and fluid flow in additive manufacturing–Part II: Powder bed fusion of stainless steel, and titanium, nickel and aluminum base alloys. Comput Mater Sci 150: 369–380. https://doi.org/10.1016/j.commatsci.2018.04.027

47. Bai X, Colegrove P, Ding J, Zhou X, Diao C, Bridgeman P, Hönnige JR, Zhang H, Williams S (2018) Numerical analysis of heat transfer and fluid flow in multilayer deposition of PAW-based wire and arc additive manufacturing. Int J Heat Mass Transf 124: 504–516. https://doi.org/10.1016/j.ijheatmasstransfer.2018.03.085

48. He X, Mazumder J (2007) Transport phenomena during direct metal deposition. J Appl Phys 101: e053113. https://doi.org/10.1063/1.2710780.

49. Lindwall G, Campbell CE, Lass EA, Zhang F, Stoudt MR, Allen AJ, Levine LE (2019) Simulation of TTT curves for additively manufactured Inconel 625. Metall Mater Trans A 50: 457–467. https://doi.org/10.1007/s11661-018-4959-7.

50. Wei HL, Knapp GL, Mukherjee T, DebRoy T (2019) Three-dimensional grain growth during multi-layer printing of a nickel-based alloy Inconel 718. Addit Manuf 25: 448–459. https://doi.org/10.1016/j.addma.2018.11.028.

51. Wei HL, Elmer JW, DebRoy T (2017) Three-dimensional modeling of grain structure evolution during welding of an aluminum alloy. Acta Mater 126: 413–425. https://doi.org/10.1016/j.actamat.2016.12.073.

52. Sun Z, Tan X, Tor SB, Chua CK (2018) Simultaneously enhanced strength and ductility for 3D-printed stainless steel 316L by selective laser melting. NPG Asia Mater 10: 127–136. https://doi.org/10.1038/s41427-018-0018-5.

53. Rai A, Markl M, Körner C (2016) A coupled Cellular Automaton–Lattice Boltzmann model for grain structure simulation during additive manufacturing. Comput Mater Sci 124: 37–48. https://doi.org/10.1016/j.commatsci.2016.07.005

54. Zhang Z, Tan ZJ, Yao XX, Hu CP, Ge P, Wan ZY, Li JY, Wu Q (2019) Numerical methods for microstructural evolutions in laser additive manufacturing. Comput Math Appl 78: 2296–2307. https://doi.org/10.1016/j.camwa.2018.07.011

55. Wang Y, Shi J, Liu Y (2019) Competitive grain growth and dendrite morphology evolution in selective laser melting of Inconel 718 superalloy. J Cryst Growth 521: 15–29. https://doi.org/10.1016/j.jcrysgro.2019.05.027

56. Kumara C, Deng D, Hanning F, Raanes M, Moverare J, Nylén P (2019) Predicting the microstructural evolution of electron beam melting of alloy 718 with phase-field modeling. Metall Mater Trans A 50: 2527–2537. https://doi.org/10.1007/s11661-019-05163-7

57. Schänzel M, Shakirov D, Ilin A, Ploshikhin V (2019) Coupled thermo-mechanical process simulation method for selective laser melting considering phase transformation steels. Comput Math Appl 78: 2230–2246. https://doi.org/10.1016/j.camwa.2019.01.019

58. Denlinger ER, Gouge M, Irwin J, Michaleris P (2017) Thermomechanical model development and in situ experimental validation of the Laser Powder-Bed Fusion process. Addit Manuf 16: 73–80. https://doi.org/10.1016/j.addma.2017.05.001

59. Shalev-Shwartz S, Ben-David S (2014) Understanding machine learning: From theory to algorithms. Cambridge University Press, Cambridge.

60. Brunton SL, Kutz JN (2019) Data-driven science and engineering: Machine learning, dynamical systems, and control. Cambridge University Press, Cambridge.

61. Bzdok D, Altman N, Krzywinski M (2018) Points of significance: statistics versus machine learning. Nat Methods 15(4): 233– 234. http://dx.doi.org/10.1038/nmeth.4642.

62. Silbernagel C, Aremu A, Ashcroft I (2020) Using machine learning to aid in the parameter optimization process for metal-based additive manufacturing. Rapid Prototyp J 26(4): 625-637. https://doi.org/10.1108/RPJ-08-2019-0213

63. Caggiano A, Zhang J, Alfieri V, Caiazzo F, Gao R, Teti R (2019) Machine learning-based image processing for on-line defect recognition in additive manufacturing. CIRP annals 68(1): 451-454. https://doi.org/10.1016/j.cirp.2019.03.021

64. Aoyagi K, Wang H, Sudo H, Chiba A (2019) Simple method to construct process maps for additive manufacturing using a support vector machine. Addit manuf 27: 353-362. https://doi.org/10.1016/j.addma.2019.03.013

65. Rankouhi B, Jahani S, Pfefferkorn FE, Thoma DJ (2021) Compositional grading of a 316L-Cu multi-material part using machine learning for the determination of selective laser melting process parameters. Addit Manuf 38: e101836. https://doi.org/10.1016/j.addma.2021.101836

66. Cao L, Li J, Hu J, Liu H, Wu Y, Zhou Q (2021) Optimization of surface roughness and dimensional accuracy in LPBF additive manufacturing. Opt Laser Technol 142: e107246. https://doi.org/10.1016/j.optlastec.2021.107246

67. Özel T, Altay A, Kaftanoğlu B, Leach R, Senin N, Donmez A (2020) Focus variation measurement and prediction of surface texture parameters using machine learning in laser powder bed fusion. J Manuf Sci Eng 142(1): e011008. https://doi.org/10.1115/1.4045415

68. Khanzadeh M, Chowdhury S, Marufuzzaman M, Tschopp MA, Bian L (2018) Porosity prediction: Supervised-learning of thermal history for direct laser deposition. J Manuf Syst 47: 69–82. https://doi.org/10.1016/j.jmsy.2018.04.001.

69. Barrionuevo GO, Ramos-Grez JA, Walczak M, Betancourt CA (2021) Comparative evaluation of supervised machine learning algorithms in the prediction of the relative density of 316L stainless steel fabricated by selective laser melting. Int J Adv Manuf Technol 113: 419–433. https://doi.org/10.1007/s00170-021-06596-4.

70. Aboutaleb AM, Mahtabi MJ, Tschopp MA, Bian L (2019) Multi-objective accelerated process optimization of mechanical properties in laser-based additive manufacturing: Case study on Selective Laser Melting (SLM) Ti-6Al-4V. J Manuf Process 38: 432-444. https://doi.org/10.1016/j.jmapro.2018.12.040

71. Hertlein N, Deshpande S, Venugopal V, Kumar M, Anand S (2020) Prediction of selective laser melting part quality using hybrid Bayesian network. Addit Manuf 32: e101089. https://doi.org/10.1016/j.addma.2020.101089.

72. Muhammad W, Brahme AP, Ibragimova O, Kang J, Inal K (2021) A machine learning framework to predict local strain distribution and the evolution of plastic anisotropy & fracture in additively manufactured alloys. Int J Plast 136: e102867. https://doi.org/10.1016/j.ijplas.2020.102867

73. Zhan Z, Li H (2021) A novel approach based on the elastoplastic fatigue damage and machine learning models for life prediction of aerospace alloy parts fabricated by additive manufacturing. Int J Fatigue 145: e106089. https://doi.org/10.1016/j.ijfatigue.2020.106089

74. Zhang M, Sun CN, Zhang X, Goh PC, Wei J, Hardacre D, Li H (2019) High cycle fatigue life prediction of laser additive manufactured stainless steel: A machine learning approach. Int J Fatigue 128: e105194. https://doi.org/10.1016/j.ijfatigue.2019.105194

75. Puichaud AH, Flament C, Chniouel A, Lomello F, Rouesne E, Giroux PF, Maskrot H, Schuster F, Béchade JL (2019) Microstructure and Mechanical Properties Relationship of Additively Manufactured 316L Stainless Steel by Selective Laser Melting. EPJ N 5: 23. https://doi.org/10.1051/epjn/2019051

76. ASTM E8/E8M-16a (2016) Standard Test Methods for Tension Testing of Metallic Materials. In: ASTM Int. West Conshohocken, PA.

77. Ladewig A, Schlick G, Fisser M, Schulze V, Glatzel U (2016) Influence of the shielding gas flow on the removal of process by-products in the selective laser melting process. Addit Manuf 10: 1-9. https://doi.org/10.1016/j.addma.2016.01.004

78. Velasco-Castro M, Hernández-Nava E, Figueroa IA, Todd I, Goodall R (2019) The effect of oxygen pickup during selective laser melting on the microstructure and mechanical properties of Ti–6Al–4V lattices. Heliyon 5(12): e02813. https://doi.org/10.1016/j.heliyon.2019.e02813

79. ASTM E407-07 (2012) Standard Practice for Microetching Metals and Alloys. In: ASTM Int. West Conshohocken, PA.

80. ASTM E112-13 (2021) Standard Test Methods for Determining Average Grain Size. In: ASTM Int. West Conshohocken, PA.

81. ASTM B311 – 17 (2017) Standard Test Method for Metallic and Inorganic Coatings, Metal Powders and Metal Powder Products. In: ASTM Int. West Conshohocken, PA.

82. ASTM E384 – 17 (2017) Standard Test Method for Micro Indentation Hardness of Materials. In: ASTM Int. West Conshohocken, PA.

83. Kullback S, Leibler RA (1951) On information and sufficiency. In: Ann math stat 22: 79–86.

84. Röttger A, Geenen K, Windmann M, Binner F, Theisen W (2016) Comparison of microstructure and mechanical properties of 316 L austenitic steel processed by selective laser melting with hot-isostatic pressed and cast material. Mater Sci Eng: A. 678: 365–376. https://doi.org/10.1016/j.msea.2016.10.012

85. Lou X, Othon MA, Rebak RB (2017) Corrosion fatigue crack growth of laser additively-manufactured 316L stainless steel in high temperature water. Corros Sci 127: 120–130. https://doi.org/10.1016/j.corsci.2017.08.023

86. Zhong Y, Liu L, Wikman S, Cui D, Shen Z (2016) Intragranular cellular segregation network structure strengthening 316L stainless steel prepared by selective laser melting. J Nucl Mater 470: 170–178. https://doi.org/10.1016/j.jnucmat.2015.12.034.

87. Zhou B, Xu P, Li W, Liang Y, Liang Y (2021) Microstructure and Anisotropy of the Mechanical Properties of 316L Stainless Steel Fabricated by Selective Laser Melting. Metals 11: e11050775. https://doi.org/10.3390/met11050775.

88. Choi JP, Shin GH, Brochu M, Kim YJ, Yang SS, Kim KT, Yang DY, Lee CW, Yu JH (2016) Densification Behavior of 316L Stainless Steel Parts Fabricated by Selective Laser Melting by Variation in Laser Energy Density. Mater Trans 57: 1952–1959. https://doi.org/10.2320/matertrans.M2016284.

89. Sun, Tan X, Tor SB, Yeong WY (2016) Selective laser melting of stainless steel 316L with low porosity and high build rates. Mater Des 104: 197–204. https://doi.org/10.1016/j.matdes.2016.05.035.

90. Wang YM, Voisin T, McKeown JT, Ye J, Calta NP, Li Z, Zeng Z, Zhang Y, Chen W, Roehling TT, Ott RT, Santala MK, Depond PJ, Matthews MJ, Hamza AV, Zhu T (2018) Additively manufactured hierarchical stainless steels with high strength and ductility. Nat Materials 17: 63–71. https://doi.org/10.1038/nmat5021.

91. Spierings AB, Starr TL, Wegener K (2013) Fatigue performance of additive manufactured metallic parts. Rapid Prototyp J 19: 88–94. https://doi.org/10.1108/13552541311302932.

92. Meier H, Haberland CH (2008) Experimental studies on selective laser melting of metallic parts. Materwiss Werksttech 39: 665–670. https://doi.org/10.1002/mawe.200800327.

93. Leuders S, Lieneke T, Lammers S, Tröster T, Niendorf T (2014) On the fatigue properties of metals manufactured by selective laser melting – The role of ductility. J Mater Res 29: 1911–1919. https://doi.org/10.1557/jmr.2014.157.

94. Li R, Liu J, Shi Y, Du M, Xie Z (2010) 316L Stainless Steel with Gradient Porosity Fabricated by Selective Laser Melting. J Mater Eng Perform 19: 666–671. https://doi.org/10.1007/s11665-009-9535-2.

95. Larimian T, Kannan M, Grzesiak D, Al-Mangour B, Borkar T (2020) Effect of energy density and scanning strategy on densification, microstructure and mechanical properties of 316L stainless steel

processed via selective laser melting. Mater Sci Eng: A. 770: e138455. https://doi.org/10.1016/j.msea.2019.138455

96. Liu J, Song Y, Chen C, Wang X, Li H, Zhou C, Wang J, Guo K, Sun J (2020) Effect of scanning speed on the microstructure and mechanical behavior of 316L stainless steel fabricated by selective laser melting. Mater Des 186: e108355. https://doi.org/10.1016/j.matdes.2019.108355.

97. Zhang B, Dembinski L, Coddet C (2013) The study of the laser parameters and environment variables effect on mechanical properties of high compact parts elaborated by selective laser melting 316L powder. Mater Sci Eng: A 584: 21–31. https://doi.org/10.1016/j.msea.2013.06.055.

98. Salman OO, Brenne F, Niendorf T, Eckert J, Prashanth KG, He T, Scudino S (2019) Impact of the scanning strategy on the mechanical behavior of 316L steel synthesized by selective laser melting. J Manuf Process 45: 255–261. https://doi.org/10.1016/j.jmapro.2019.07.010.

99. Song Y, Sun Q, Guo K, Wang X, Liu J, Sun J (2020) Effect of scanning strategies on the microstructure and mechanical behavior of 316L stainless steel fabricated by selective laser melting. Mater Sci Eng: A. 793: e139879. https://doi.org/10.1016/j.msea.2020.139879.

100. Alsalla HH, Smith C, Hao L (2018) Effect of build orientation on the surface quality, microstructure and mechanical properties of selective laser melting 316L stainless steel. Rapid Prototyp J 24: 9–17. https://doi.org/10.1108/RPJ-04-2016-0068.

101. Ma M, Wang Z, Zeng X (2017) A comparison on metallurgical behaviors of 316L stainless steel by selective laser melting and laser cladding deposition. Mater Sci Eng: A 685: 265–273. https://doi.org/10.1016/j.msea.2016.12.112.

102. Peng T, Chen C (2018) Influence of energy density on energy demand and porosity of 316L stainless steel fabricated by selective laser melting. Int J Pr Eng Man-Gt 5: 55–62. https://doi.org/10.1007/s40684-018-0006-9.

103. Yadroitsev I, Smurov I (2010) Selective laser melting technology: from the single laser melted track stability to 3D parts of complex shape. Phys Procedia 5: 551–560. https://doi.org/10.1016/j.phpro.2010.08.083.

104. Dadbakhsh S, Hao L, Sewell N (2012) Effect of selective laser melting layout on the quality of stainless-steel parts. Rapid Prototyp J 18: 241-249. https://doi.org/10.1108/13552541211218216.

105. Deng Y, Mao Z, Yang N, Niu X, Lu X (2020) Collaborative Optimization of Density and Surface Roughness of 316L Stainless Steel in Selective Laser Melting. Materials 13: e13071601. https://doi.org/10.3390/ma13071601.

106. Wang D, Liu Y, Yang Y, Xiao D (2016) Theoretical and experimental study on surface roughness of 316L stainless steel metal parts obtained through selective laser melting. Rapid Prototyp J 22: 706–716. https://doi.org/10.1108/RPJ-06-2015-0078.

107. Yang X, Ren Y, Liu S, Wang Q, Shi M (2020) Microstructure and tensile property of LPBF 316L stainless steel manufactured with fine and coarse powder mixtures. J Cent South Univ 27: 334–343. https://doi.org/10.1007/s11771-020-4299-9.

108. Casati R, Lemke J, Vedani M (2016) Microstructure and Fracture Behavior of 316L Austenitic Stainless Steel Produced by Selective Laser Melting. J Mater Sci Technol 32: 738–744. https://doi.org/10.1016/j.jmst.2016.06.016.

109. Liverani E, Lutey AHA, Ascari A, Fortunato A (2020) The effects of hot isostatic pressing (HIP) and solubilization heat treatment on the density, mechanical properties, and microstructure of austenitic stainless-steel parts produced by selective laser melting (LPBF). Int J Adv Manuf Technol 107: 109–122. https://doi.org/10.1007/s00170-020-05072-9.

110. Cacace S, Demir AG, Semeraro Q (2017) Densification Mechanism for Different Types of Stainless-Steel Powders in Selective Laser Melting. Procedia CIRP 62: 475–480. https://doi.org/10.1016/j.procir.2016.06.010.

111. Lavery NP, Cherry J, Mehmood S, Davies H, Girling B, Sackett E, Brown SGR, Sienz J (2017) Effects of hot isostatic pressing on the elastic modulus and tensile properties of 316L parts made by powder bed laser fusion. Mater Sci Eng: A 693: 186–213. https://doi.org/10.1016/j.msea.2017.03.100.

112. Cacace S, Semeraro Q (2020) Influence of the atomization medium on the properties of stainless steel SLM parts. Addit Manuf 36: e101509. https://doi.org/10.1016/j.addma.2020.101509.

113. Yu C, Zhao C, Zhang Z, Liu W (2019) Tensile Properties of Selective Laser Melted 316L Stainless Steel. Acta Metall Sin 56: 683–692. https://doi.org/10.11900/0412.1961.2019.00278.

114. Brytan Z. (2017) Comparison of Vacuum Sintered and Selective Laser Melted Steel AISI 316L Arch Metall Mater 62: 2125–2131. https://doi.org/10.1515/amm-2017-0314.

115. Woźniak A, Adamiak M, Chladek G, Kasperski J (2020) The Influence of the Process Parameters on the Microstructure and Properties SLM Processed 316L Stainless Steel. Arch Metall Mater 65: e131098. http://dx.doi.org/10.24425/amm.2019.131098.

116. Kale AB, Kim BK, Kim DI, Castle EG, Reece M, Choi SH (2020) An investigation of the corrosion behavior of 316L stainless steel fabricated by SLM and SPS techniques. Mater Charact 163: e110204. https://doi.org/10.1016/j.matchar.2020.110204

117. Huang Z, Qi W, Zhou Y, Xu C, Zhang Z, Liu J, Hu G (2017) Effect of Print Method Based on SLM Technology on the Microstructure and Property of 316L Stainless Steel. In: Chinese Mater Conf. pp.157-164.

118. Sun Y, Moroz A, Alrbaey K (2014) Sliding Wear Characteristics and Corrosion Behaviour of Selective Laser Melted 316L Stainless Steel. J Mater Eng Perform 23: 518–526. https://doi.org/10.1007/s11665-013-0784-8.

119. Lin K, Gu D, Xi L, Yuan L, Niu S, Lv P, Ge Q (2019) Selective laser melting processing of 316L stainless steel: effect of microstructural differences along building direction on corrosion behavior. J Adv Manuf Technol 104: 2669–2679. https://doi.org/10.1007/s00170-019-04136-9.

120. Chu B, Zhang Z, Yang Z (2018) Influence of SLM molding angle on tensile properties of 316L stainless steel forming parts. In: AIP Conf Proc 1967 (1): p. 030041.

121. Ding H, Tang Q, Zhu Y, Zhang C, Yang H (2021) Cavitation erosion resistance of 316L stainless steel fabricated using selective laser melting. Friction 9: 1580–1598. https://doi.org/10.1007/s40544-020-0443-7.

122. Liu B, Wildman R, Tuck C, Ashcroft I, Hague R (2011) Investigation the effect of particle size distribution on processing parameters optimization in selective laser melting process. In: 2011 Int Solid Free Fabr Symp SFF.

123. Laohaprapanon A, Jeamwatthanachai P, Wongcumchang M, Chantarapanich N, Chantaweroad S, Sitthiseripratip K, Wisutmethangoon S (2011) Optimal Scanning Condition of Selective Laser Melting Processing with Stainless Steel 316L Powder. Adv Mater Res 341: 816–820. https://doi.org/10.4028/www.scientific.net/AMR.341-342.816.

124. Huang Y, Yang S, Gu J, Xiong Q, Duan C, Meng X, Fang Y (2020) Microstructure and wear properties of selective laser melting 316L. Mater Chem Phys 254: 123487. https://doi.org/10.1016/j.matchemphys.2020.123487.

125. Yang X, Liu Y, Ye J, Wang R, Zhou T, Mao B (2019) Enhanced mechanical properties and formability of 316L stainless steel materials 3D-printed using selective laser melting. Int J Miner Metall Mater 26: 1396–1404. https://doi.org/10.1007/s12613-019-1837-2.

126. Montuori RAM, Figueira G, Cataldi TP, de Alcântara NG, Bolfarini C, Coelho RT, Gargarella P (2020) Additive Manufacturing of 316L stainless steel by Selective Laser Melting. Soldag insp 25. https://doi.org/10.1590/0104-9224/SI25.30

127. Burnham KP, Anderson DR (2002) A practical information-theoretic approach, Model Selection and Multimodel Inference. Springer, New York.

128. Akaike H (1978) A new look at the statistical model identification. Automatica 19: 465–471.

129. Schwarz G (1978) Estimating the dimension of a model. Ann Stat 461–464.

130. Minkowski H, Geometrie der Zahlen (retrieved 2016-02-28, 1910) Leipzig and Berlin: RG Teubner. JFM 41.0239. 03. MR 0249269.

131. Mahalanobis PC (1936) On the generalized distance in statistics. National Institute of Science of India.

132. Donoho DL (2006) For most large underdetermined systems of linear equations the minimal 1-norm solution is also the sparsest solution. Commun Pure Appl Math 59: 797–829. https://doi.org/10.1002/cpa.20132.

133. Keller JM, Gray MR, Givens JA (1985) A fuzzy k-nearest neighbor algorithm. IEEE Trans Syst, Man, Cybern 15(4):258-63.

134. Altman NS (1992) An Introduction to Kernel and Nearest-Neighbor Nonparametric Regression. Am Stat 46: 175–185. https://doi.org/10.1080/00031305.1992.10475879.

135. Cortes C, Vapnik V (1995) Support-vector networks. Mach Learn 20: 273–297. https://doi.org/10.1007/BF00994018.

136. Freund Y, Schapire RE (1997) A decision-theoretic generalization of on-line learning and an application to boosting. J Comput Syst Sci 55: 119–139.

137. MATLAB (2020b) Version: 9.9.0.1467703 (R2020b). The MathWorks Inc. Natick, Massachusetts.

138. The MathWorks I (2020b) Statistics and Machine Learning Toolbox. Natick, Massachusetts. https://www.mathworks.com/help/stats/

139. Eshkabilov S (2019) Beginning MATLAB and Simulink. Springer.

140. Ara I, Azarmi F, Tangpong XW (2021) Microstructure Analysis of High-Density 316L Stainless Steel Manufactured by Selective Laser Melting Process. Metallogr Microstruct Anal 10(6): 754-767.

141. Eshkabilov S, Ara I, Sevostianov I, Azarmi F, Tangpong X (2021) Mechanical and thermal properties of stainless-steel parts, manufactured by various technologies, in relation to their microstructure. Int J Eng Sci 159: e103398.

142. Ara I, Eshkabilov S, Azarmi F, Sevostianov I, Tangpong XW (2022) Investigation on elastic properties and unconventional plasticity of 316L stainless steel processed by selective laser melting technology. Prog Addit Manuf: 1-13.

143. Fan RE, Chen PH, Lin CJ (2005) Working set selection using second order information for training support vector machines. J Mach Learn Res 6: 1889–1918.

144. Gould N, Toint PL (2004) Preprocessing for quadratic programming. Math Program Ser B 100: 95–132. https://doi.org/10.1007/s10107-003-0487-2.

Supplementary Files

This is a list of supplementary files associated with this preprint. Click to download.

- DATA316ALL.xlsx